



# Melting experiments on the Fe–C binary system up to 255 GPa: Constraints on the carbon content in the Earth's core

Izumi Mashino, Francesca Miozzi, Kei Hirose, Guillaume Morard, Ryosuke Sinmyo

## ► To cite this version:

Izumi Mashino, Francesca Miozzi, Kei Hirose, Guillaume Morard, Ryosuke Sinmyo. Melting experiments on the Fe–C binary system up to 255 GPa: Constraints on the carbon content in the Earth's core. *Earth and Planetary Science Letters*, 2019, 515, pp.135-144. 10.1016/j.epsl.2019.03.020 . hal-02180578

**HAL Id: hal-02180578**

**<https://hal.sorbonne-universite.fr/hal-02180578v1>**

Submitted on 11 Jul 2019

**HAL** is a multi-disciplinary open access archive for the deposit and dissemination of scientific research documents, whether they are published or not. The documents may come from teaching and research institutions in France or abroad, or from public or private research centers.

L'archive ouverte pluridisciplinaire **HAL**, est destinée au dépôt et à la diffusion de documents scientifiques de niveau recherche, publiés ou non, émanant des établissements d'enseignement et de recherche français ou étrangers, des laboratoires publics ou privés.

**Melting experiments on the Fe–C binary system up to 255 GPa:**

**Constraints on the carbon content in the Earth's core**

Izumi Mashino <sup>a,\*</sup>, Francesca Miozzi <sup>b</sup>, Kei Hirose <sup>a,c</sup>, Guillaume Morard <sup>b</sup>, Ryosuke Sinmyo <sup>a</sup>

<sup>a</sup>Department of Earth and Planetary Science, The University of Tokyo, Hongo, Tokyo, 113-0033, Japan

<sup>b</sup>Sorbonne Université, Muséum National d'Histoire Naturelle, UMR CNRS 7590, IRD, Institut de Minéralogie, de Physique des Matériaux et de Cosmochimie, IMPMC, 75005 Paris, France

<sup>c</sup>Earth-Life Science Institute, Tokyo Institute of Technology, Meguro, Tokyo 152-8550, Japan

\*Corresponding author.

*E-mail address:* [izumi.mashino@erdw.ethz.ch](mailto:izumi.mashino@erdw.ethz.ch) (I. Mashino, Now at ETH)

## ABSTRACT

Phase relations, including the eutectic liquid composition in the Fe–C binary system, remain unclear under the core pressure range, which makes estimating the carbon budget in the Earth’s core difficult. To explore this issue, we have conducted melting and subsolidus experiments on Fe–C alloys in a diamond-anvil cell up to 255 GPa. Textural and compositional characterizations of quenched samples show that carbon concentration in the eutectic liquid slightly decreases with increasing pressure and is about 3 wt.% at the inner core boundary (ICB) pressure. The solubility of carbon in solid Fe is found to be almost constant at ~1.0 wt.%. *In situ* X-ray diffraction data indicate that Fe forms eutectic melting with Fe<sub>3</sub>C to 203 GPa and with Fe<sub>7</sub>C<sub>3</sub> at 255 GPa.

Previous studies on liquid Fe–C alloys suggested that the density of the outer core is explained by liquid Fe containing 1.8 to 4.2 wt.% C. If the liquid core includes <3 wt.% C as a single light element, hexagonal close-packed (hcp) Fe crystallizes at the ICB. However, the carbon content in such solid Fe is  $\leq 1$  wt.%, less than that required to account for the inner core density deficit from pure iron. When the outer core includes  $\geq 3$  wt.% C, it forms Fe<sub>7</sub>C<sub>3</sub> at the ICB, whose density is too small for the inner core. Carbon is therefore not a primary light element in the core. Nevertheless, the outer core liquid can be Fe–C–Si, Fe–C–S, or Fe–C–H. Such core liquid crystallizes solid Fe with light elements including less than 1 wt.% C, which may explain the density and the sound velocities observed in the inner core.

**Keywords:** core; iron alloy; carbon; eutectic liquid; high pressure

## 1. Introduction

Carbon has been believed to be one of feasible light elements contained in planetary cores because of its high abundance in the solar system and strong affinity to molten iron (Benz and Elliott, 1961; Anders and Grevesse, 1989; Wood, 1993). Recent first-principles calculations predicted that the incorporation of a small amount of carbon in hcp Fe is compatible with the density and sound velocities observed in the Earth's inner core (Li et al., 2018).

In order to reveal the abundance of carbon in the core, it is important to understand the Fe–C phase diagram at high pressure, in particular at 330 GPa, which corresponds to the conditions at the ICB. Wood (1993) first thermodynamically calculated the phase relations in the Fe–C system up to 136 GPa and predicted that the Earth's core could contain ~4 wt.% C. Nakajima et al. (2009) experimentally determined the melting phase relationships in the Fe-rich portion of the Fe–C system up to 29 GPa and demonstrated that Fe<sub>7</sub>C<sub>3</sub> appears as a liquidus phase. Using an *in situ* X-radiographic imaging technique, Lord et al. (2009) found that carbon concentration in the eutectic liquid in the Fe–C binary system decreases substantially with increasing pressure to 70 GPa. The thermodynamic modeling by Fei and Brosh (2014) based on multi-anvil experiments up to 25 GPa predicted that the Fe–C eutectic liquid composition includes 2.2 wt.% C at 330 GPa. More recently Morard et al. (2017a) reported the change in carbon concentration in the eutectic liquid in the Fe–Fe<sub>3</sub>C binary up to 107 GPa and estimated it to be 2.6 wt.% C at the core–mantle boundary (CMB). However, they obtained liquid compositions from X-ray diffraction (XRD) patterns with the Rietveld method, which includes great uncertainty. So far, melting experiments on the Fe–C system have not been carried out under the core pressure range (>136 GPa). Moreover, the solubility of



carbon in solid iron also remains unknown above 25 GPa (Chabot et al., 2008; Walker et al., 2013; Fei and Brosh, 2014).

It is also important to verify the change in liquidus phase in the Fe–C system. It has been suggested that the liquidus field of  $\text{Fe}_7\text{C}_3$  expands with respect to that of  $\text{Fe}_3\text{C}$  and eutectic melting occurs between Fe and  $\text{Fe}_7\text{C}_3$  above 120 GPa (Lord et al., 2009; Fei and Brosh, 2014). Furthermore, the recent experiments by Liu et al. (2016) showed the decomposition of  $\text{Fe}_3\text{C}$  into Fe +  $\text{Fe}_7\text{C}_3$  above 145 GPa, but it contradicts the formation of  $\text{Fe}_3\text{C}$  at >300 GPa and >5000 K reported by Tateno et al. (2010).  $\text{Fe}_7\text{C}_3$  has been regarded as a possible constituent in the inner core because it provides a good match for both compressional ( $V_P$ ) and shear velocities ( $V_S$ ) (or Poisson's ratio) of the inner core under relevant conditions (Nakajima et al., 2009; Mookherjee et al., 2011; Chen et al., 2014; Prescher et al., 2015). The calculations by Li et al. (2016), however, demonstrated that the density of  $\text{Fe}_7\text{C}_3$  is too small for the inner core.

Recent progress in melting experiments in a diamond-anvil cell (DAC) combined with a focused ion beam (FIB) technique has enabled us to determine the eutectic liquid composition to the core pressure range (Ozawa et al., 2016; Mori et al., 2017; Hirose et al., 2017). In this study, we have conducted both subsolidus and melting experiments on Fe–C alloys up to 255 GPa in order to determine the change in melting phase relations with increasing pressure, in particular 1) the stability of  $\text{Fe}_7\text{C}_3$  at liquidus, 2) carbon concentration in eutectic liquid, and 3) the solubility of carbon in solid iron. Based on these results, we discuss the possible carbon content in the Earth's core and the mineralogy of the inner core.

## 2. Experimental methods

High-pressure and -temperature ( $P$ - $T$ ) conditions were generated in a laser-heated DAC using double-, single-beveled, and flat diamond anvils with 60, 90, 150, and 300  $\mu\text{m}$  culet size. Starting materials were foils of Fe containing 1.9 wt.% C and 4.0 wt.% C, which are homogeneous mixtures of fine-grained Fe and  $\text{Fe}_3\text{C}$  synthesized by an ultra-rapid quenching method (Morard et al., 2011, 2017a). Rhenium gaskets were pre-indented to about 40  $\mu\text{m}$  thickness before laser drilling or spark erosion of sample holes with 30–100  $\mu\text{m}$  diameters. Sample pellets were loaded between two pieces of about 10  $\mu\text{m}$  thick dry  $\text{Al}_2\text{O}_3$ , which served as a pressure-transmitting medium and a thermal insulator from the diamond anvils. After loading, the whole DAC was dried in a vacuum oven at 423 K for more than 12 hrs, and subsequently a sample chamber was flushed with dry argon and squeezed in an argon atmosphere.

After compression to a desired pressure, the sample was heated from both sides with a couple of 100-W single-mode Yb fiber lasers. We used beam-shaping optics, which converts a Gaussian beam to one with a flat energy distribution and thus reduces radial temperature gradient in the sample. A laser-heated spot was up to  $\sim 20$   $\mu\text{m}$  across. One-dimensional temperature distributions on the surface of the sample were obtained using a spectro-radiometric method (Ohishi et al., 2008). Heating duration was limited to about 5 s in order to avoid fluctuations in temperature, which would otherwise cause complex melting textures. The experimental temperature reported in this study is that at the solid/liquid boundary, which is obtained by combining the measured radial temperature distribution with the melting texture observed in a sample's cross section (Fig. 1) (see Ozawa et al., 2016 for details). We polished the sample using an FIB from both sides little by little ( $\sim 1$   $\mu\text{m}$  for each step) in order to have a cross section at the center of a liquid pool. The sample was thinned to about 3  $\mu\text{m}$  thickness at the end. The

uncertainty in temperature is  $\pm 5$  % according to Mori et al. (2017), which includes uncertainties in the width of the liquid pool as well as those derived from the facts that we calculated temperature from integrated light not only from the sample surface but also from the pressure medium and that spatial resolution of the temperature profile was 2 to 3  $\mu\text{m}$ .

Pressure at room temperature was obtained based on the Raman shift of a diamond anvil (Akahama and Kawamura, 2004). It was then corrected for a contribution of thermal pressure. According to Andraut et al. (1998), when purely isochoric heating is made, the thermal pressure is written as  $\Delta P = \alpha K_T T$ , in which  $\alpha$  is thermal expansivity and  $K_T$  is isothermal bulk modulus. Assuming the thermal parameters for liquid Fe-C same as those for pure iron, we employ  $\alpha K_T = 9$  MPa/K (Ichikawa et al., 2014) for runs performed above 83 GPa. Andraut et al. (1998) demonstrated that 90% of such isochoric thermal pressure contributes to an experimental pressure increase at the core pressure range. For runs #1, #2, and #5 conducted at relatively low pressures, the lower  $\alpha K_T$  value of 4 MPa/K and 60% of the theoretical value were applied (Morard et al., 2011; Andraut et al., 1998). The overall errors in pressure should be less than  $\pm 10$  % in the present experiments including the uncertainty in thermal pressure estimate, as argued in Mori et al. (2017). Indeed, we found 191 GPa at 2300 K in run #7 based on the volume and equation of state (EoS) of  $\text{Fe}_3\text{C}$  (Sata et al., 2010), which is consistent with 194 GPa calculated with the thermal pressure correction.

Synchrotron XRD measurements were carried out *in situ* at high  $P$ - $T$  in runs #7 and #8 at BL10XU, SPring-8 (Ohishi et al., 2008) using an X-ray beam with an energy of  $\sim 30$  keV. Angle-dispersive XRD spectra were collected on a flat panel detector (Perkin Elmer) with typical exposure time of 200 ms. A monochromatic incident X-ray

beam was collimated to 2  $\mu\text{m}$  (FWHM). Visible fluorescent light induced by X-rays in a diamond was used to precisely align the laser-heated spot with the X-ray beam. Two-dimensional XRD images were integrated to produce a conventional one-dimensional diffraction profile using the IPAnalyzer software (Seto et al., 2010).

Recovered samples from our DAC experiments were cross-sectioned using a  $\text{Ga}^+$  focused ion beam (FIB) instrument (FEI VersaTM3D DualBeamTM). During FIB sectioning, sample was monitored by scanning electron microscopy using back-scattered electrons to precisely section the center of a heated spot. The sample cross sections were then examined by a field-emission-type scanning electron microscope (FE-SEM) and energy dispersive X-ray spectrometry (EDS) with a silicon drift detector. The section was then mounted on a Cu grid and further thinned to approximately 3  $\mu\text{m}$  thickness for further analysis with a field-emission-type electron probe microanalyzer (FE-EPMA, JXA-8530F, JEOL) in order to determine chemical compositions. Since Fe-C samples are good electric conductors, no coating material was necessary for EPMA analysis with an accelerating voltage of 10 kV and a beam current of 15 nA. A focused electron beam for spot analyses was less than 50 nm in size. We used both  $\text{Fe}_3\text{C}$  and  $\text{Fe}_7\text{C}_3$  as standards that were synthesized at 5 GPa/1473 K and applied the ZAF correction (Nakajima et al., 2009). Corundum (for Al and O) and pure iron (for Fe) were also used for standards. The X-ray counting time for peak/background was 20s/10s. LDE2 (C), TAP (Al), LIFH (Fe), and LDE1H (O) were analyzing crystals.

Very minor amounts of aluminum and oxygen were found when analyzing the sample, most likely due to a signal from a neighboring/underlying  $\text{Al}_2\text{O}_3$  insulation layer. We estimated the carbon concentrations in quenched liquid and solid metals after subtracting  $\text{Al}_2\text{O}_3$  from raw analyses. In addition, we analyzed two samples (runs #2 &

#6) by EPMA with a liquid nitrogen cold finger (JXA-8530FPlus HyperProbe Electron Probe Microanalyzer) at both 10 kV and 15 kV accelerating voltage (Table S1). The results demonstrate that the carbon contents obtained with and without the cold finger are similar to each other. We repeated the analyses of the Fe<sub>3</sub>C standard twenty times and found that the carbon concentration changed only by  $\pm 0.1766$  atm%. While chemical compositions were calculated by using both the 'standard' ZAF correction and the phi-rho-z type procedure, the results are consistent with each other (see Table S1).

### 3. Results

#### 3.1. Carbon contents in eutectic liquid and coexisting solid iron

We have conducted eight separate DAC runs for melting experiments in a pressure range from 23 GPa to 255 GPa (Table 1). Figs. 1 and 2 show typical melting textures on recovered samples. There is a chemically homogeneous part at the center of a laser-heating spot, which is non-stoichiometric in composition and should represent a quenched liquid. The liquidus phase (solid phase in contact with liquid) is found at both sides of the liquid. The outermost low-temperature area remained subsolidus. We observed iron carbide (Fe<sub>3</sub>C or Fe<sub>7</sub>C<sub>3</sub>) or metallic iron (or both) as liquidus phase(s). In runs #2, #4, #5, and #8, both iron carbide and iron were present, suggesting that the quenched liquid in these runs may represent a eutectic liquid in the Fe–C binary system. Carbon diffusivity in liquid iron was estimated to be about  $10^{-8}$  m<sup>2</sup>/s under the present *P-T* conditions (Helffrich, 2014), indicating that 1 s is long enough for carbon to diffuse in the present liquid pool that was less than 20  $\mu$ m across (Figs. 1 and 2). Since melting/crystallization at the liquid/solid boundary occurs almost instantaneously, chemical homogeneity in the liquid assures that chemical equilibrium was attained in

the present heating duration of about 5 s. The Fe-C liquids obtained in the core pressure range included about 1 wt.% oxygen in addition to carbon (Table 1), which might have affected phase relations in the Fe-C binary system.

We determined the carbon concentration in quenched liquid up to 255 GPa, the conditions corresponding to the middle of the outer core, more than twice the pressure compared to previous experimental studies (e.g., Lord et al., 2009; Fei and Brosh, 2014; Morard et al., 2017a). Fig. 3 demonstrates the carbon concentrations in liquids as a function of pressure, which constrains the change in eutectic liquid composition, considering that they indicate the lower and upper bounds for the carbon content in eutectic liquid at each pressure when coexisting with iron and iron carbides, respectively. These data show a small reduction in carbon content in the eutectic liquid with increasing pressure above 23 GPa. Our results are not consistent with the continuous reduction that was thermodynamically predicted by Fei and Brosh (2014) and experimentally reported by Lord et al. (2009) (Fig. 3). The difference from Lord et al. (2009) may be attributed to the difference in analytical method: Lord and others employed an X-radiographic imaging technique for chemical analysis, while we based our measurements on electron microprobe analyses.

We also obtained the carbon concentrations in solid iron coexisting with Fe-C liquid as a function of pressure (Fig. 4). Liquid Fe-C coexists with face-centered cubic (fcc) iron at relatively low pressure range, in which carbon atoms occupy the octahedral interstitial sites (Fei and Brosh, 2014). Previous studies reported that the maximum solubility of carbon in fcc-Fe is <2.1 wt.% at 1 bar and predicted that it decreases at higher pressures (Walker et al., 2013; Fei and Brosh, 2014). Our results show about 1.0 wt.% in fcc-Fe from 23 to 54 GPa, in good agreement with such predictions. Above 138

GPa in the present experiments, hcp Fe should have crystallized from Fe-C liquid and again included 1.0 wt.% or less C. The effect of pressure on the solubility of carbon in hcp Fe was not observed.

### 3.2. Eutectic temperature in the Fe–C system

The temperature at the solid/liquid boundary gives the upper bound for eutectic temperature. These temperatures are plotted as a function of pressure in Fig. 5a, which constrains the eutectic melting curve to mid-outer core pressures. We fit the Simon-Glatzel equation to the data (Simon and Glatzel, 1929):

$$T_m = T_{mref} \left( \frac{P - P_{ref}}{a} + 1 \right)^{1/c} \quad (1)$$

where  $T_m$  is eutectic temperature, and both  $a$  and  $c$  are fitting parameters.  $T_{mref} = 1513$  K at  $P_{ref} = 5$  GPa is employed as a reference eutectic temperature from previous data obtained using a large-volume press (Fei and Brosh, 2014). The best fitted parameters are  $a = 8.4 \pm 3.3$  GPa and  $c = 4.1 \pm 0.5$ . The obtained eutectic melting curve shown in Fig. 5a is consistent with those of previous studies by Liu et al. (2016) and Morard et al. (2017a) within experimental uncertainties. Fig. 5b compares the eutectic melting curves of iron alloys. Under the core pressure range, the Fe–C system exhibits a eutectic temperature lower than those of Fe (Anzellini et al., 2013), Fe–FeSi (Fischer et al., 2013), and Fe–FeO (Morard et al., 2017a). And, the Fe–C eutectic melting temperature is higher than that in Fe–Fe<sub>3</sub>S below ~250 GPa, but is lower at higher pressures including the ICB pressure (Mori et al., 2017).

### 3.3. Liquidus field of Fe<sub>7</sub>C<sub>3</sub>

In runs #7 and #8 using the Fe-4.0 wt.%C starting material, the sample was initially compressed at room temperature to 176 GPa and 226 GPa, respectively (Fig. 6). Broad XRD peaks from hcp Fe and Fe<sub>3</sub>C were observed before heating in both runs. The peaks from both phases became sharper and spotty upon heating to 2300 K in run #7, in which more than 10 peaks were indexed to Fe<sub>3</sub>C cementite (Sata et al., 2010), and only Fe<sub>3</sub>C phase was observed from the sample in the XRD pattern during melting at 203 GPa and 3350 K. In addition, we confirmed with an FE-EPMA that the quenched liquid was surrounded by Fe<sub>3</sub>C in the recovered sample (Fig. 7a). These indicate that Fe forms eutectic melting with Fe<sub>3</sub>C at 203 GPa.

In the case of run #8, the diffraction peaks from hcp Fe and Fe<sub>3</sub>C became sharper and spotty upon heating. We then observed the appearance of the peaks that are assigned to Fe<sub>7</sub>C<sub>3</sub> (orthorhombic, *Pbca*) (Prescher et al., 2015) after we melted the sample by increasing temperature to 3570 K at 255 GPa. After quenching this sample, we confirmed with the FE-EPMA that the liquid was in contact with both Fe and Fe<sub>7</sub>C<sub>3</sub>, whereas the subsolidus part was composed of Fe and Fe<sub>3</sub>C (Fig. 7b). These show that eutectic melting occurs between Fe and Fe<sub>7</sub>C<sub>3</sub> at 255 GPa. This observation is not consistent with Liu et al. (2016), who argued that Fe<sub>3</sub>C dissociates into Fe + Fe<sub>7</sub>C<sub>3</sub> at subsolidus above 145 GPa when using Fe<sub>3</sub>C as a sample. Liu and others based their conclusions purely on the change in XRD patterns, and they may have collected them above eutectic temperature.

## **4. Discussion**

### *4.1. Phase diagram of Fe–C system at ICB*



The eutectic liquid composition (Fig. 3) and eutectic melting curve obtained in this study (Fig. 5) indicate that eutectic melting occurs in Fe–Fe<sub>3</sub>C at Fe + 3.5 wt.% C at 135 GPa and 3000 K. And, these data determined up to 255 GPa suggest that the eutectic liquid includes about 3 wt.% C at 330 GPa and 3750 K.

We model the liquidus curve for the Fe-rich side of the eutectic to 330 GPa (Fig. 8). Considering an ideal solution, a molar ratio of Fe in liquid at  $T$  is given by:

$$\chi_{\text{Fe liq}} = \exp \left\{ \frac{\bar{G}_{\text{Fe sol}}^0 - \bar{G}_{\text{Fe liq}}^0}{RT} \right\} = \exp \left\{ - \int_{T_{m \text{ Fe}}}^T \frac{\bar{H}_{\text{Fe sol}}^0 - \bar{H}_{\text{Fe liq}}^0}{RT^2} dT \right\} \quad (2)$$

where  $\bar{G}_{\text{Fe } i}^0$  and  $\bar{H}_{\text{Fe } i}^0$  are standard Gibbs free energy and the enthalpy of phase  $i$ , respectively,  $T_{m \text{ Fe}}$  is the melting temperature of pure Fe, and  $R$  is gas constant. When we assume that an enthalpy change upon fusion,  $\bar{H}_{\text{Fe liq}}^0 - \bar{H}_{\text{Fe sol}}^0$ , is independent from temperature, Eq. (2) is written as:

$$\chi_{\text{Fe liq}} = \exp \left\{ \left( \frac{\bar{H}_{\text{Fe liq}}^0 - \bar{H}_{\text{Fe sol}}^0}{RT_{m \text{ Fe}}} \right) \times \left( 1 - \frac{T_{m \text{ Fe}}}{T} \right) \right\} = \exp \left\{ A \times \left( 1 - \frac{T_{m \text{ Fe}}}{T} \right) \right\} \quad (3)$$

Here  $A$  is constant and calculated from  $T_{m \text{ Fe}}$  (Anzellini et al., 2013), eutectic temperature, and eutectic composition (Figs. 3 and 5) at a given pressure (see also Mori et al., 2017).

#### 4.2. Fe–C core liquid?

Melting phase relations in the Fe–C system constrain the carbon budget in the Earth's core and the mineralogy of the solid inner core. The maximum carbon content in the outer core has been estimated from the core density deficit. Recent experimental and computational studies on the density of liquid Fe–C alloys indicate 1.8 to 4.2 wt.% C in the liquid core at the ICB (Badro et al., 2014; Nakajima et al., 2015; Morard et al., 2017b), although earlier estimates based on the EoS of solid Fe<sub>3</sub>C suggested higher

carbon concentration (7.7–9.2 wt.% C) (Sata et al., 2010). Since the eutectic point is located at about 3 wt.% C at 330 GPa (Fig. 8), if the Fe-C outer core includes less than 3 wt.% C, it crystallizes hcp Fe with  $\leq 1$  wt.% C at the ICB (Fig. 4). In this case, however, the difference in carbon concentration between the liquid and solid core is too small to explain the density jump (4.5 to 6.5%) across the ICB (Shearer and Masters, 1990; Masters and Gubbins, 2003). Moreover, assuming a linear density change between pure Fe (Sakamaki et al., 2016), Fe<sub>3</sub>C (Sata et al., 2010), and Fe<sub>7</sub>C<sub>3</sub> (Prescher et al., 2015), hcp Fe with 1.0 wt.% C is found to be only 1.3% lighter than pure iron, which is not enough to account for the inner core density deficit of 4–6% (Brown and McQueen, 1986; Shearer and Masters, 1990; Masters and Gubbins, 2003; Dewaele et al., 2006; Komabayashi and Fei, 2010). This is supported by the recent calculations by Li et al. (2018). Less than 3 wt.% C as a single light element in the core is therefore unlikely.

Next we consider the case that the liquid core contains more than 3 wt.% C as the sole light component, from which Fe<sub>7</sub>C<sub>3</sub> crystallizes at the ICB (Fig. 8). It has been suggested that both  $V_P$  and  $V_S$ —in particular the slow  $V_S$  (high Poisson’s ratio)—of the inner core could be reconciled with non-magnetic Fe<sub>7</sub>C<sub>3</sub> (Mookherjee et al., 2011; Chen et al., 2014; Prescher et al., 2015). If the inner core is composed of solid Fe<sub>7</sub>C<sub>3</sub>, the liquid outer core should include 5.4–6.7 wt.% C according to Badro et al. (2014) or 5.2–6.0 wt.% C based on Nakajima et al. (2015), considering that the outer core should be 4.5–6.5% less dense than solid Fe<sub>7</sub>C<sub>3</sub> (Chen et al., 2014). More than 5 wt.% C in liquid iron, however, leads to a bulk sound velocity and a density much higher and lower than those observed for the outer core, respectively (Badro et al., 2014; Nakajima et al., 2015; Morard et al., 2017b) and is thus unlikely. The computational study by Li et al.

(2016) also showed that the density of  $\text{Fe}_7\text{C}_3$  is too low to be a major constituent of the inner core.

These suggest that carbon cannot be a predominant light element in the outer core. It is indeed consistent with Wood et al. (2013), who proposed that the maximum carbon content in the core is 1.0 wt.%, which was deduced from the carbon isotopic signature in silicate Earth and the silicate-metal fractionation factors. It has also been argued that the outer core velocity is explained by the incorporation of a small amount of carbon that is not enough to account for its density deficit from pure iron (Badro et al., 2014; Nakajima et al., 2015).

#### 4.3. *Fe-C-X core liquid?*

Furthermore, we consider the Fe-C-X (X = Si, S, O, or H) ternary systems to seek possible ranges of outer core composition, from which hcp Fe crystallizes (Figs. 9a–d). The eutectic liquid composition in each Fe–X binary system has been estimated to be Fe with 3 wt.% C (this study), 1.5 wt.% Si (Ozawa et al., 2016), 5 wt.% S (Mori et al., 2017), and >10 wt.% O (Morard et al., 2017a) at 330 GPa. The hydrogen concentration in the Fe–H eutectic liquid is unclear, but it would be around 1 wt.% H according to Fukai (1992) and Shibazaki et al. (2014). The ternary eutectic points in these systems are not exactly known, but the recent melting experiments performed by Tateno et al. (2018) have demonstrated that the Fe–Si–S ternary eutectic point is located 1) near the tie line between the Fe–FeSi and Fe–Fe<sub>3</sub>S binary eutectic points and 2) close to the Fe–Fe<sub>3</sub>S binary join because the eutectic temperature in Fe–Fe<sub>3</sub>S is much lower than that in Fe–FeSi. The present data show that the eutectic temperature in the Fe–C binary system is low compared to those in other systems (Fe–Si, Fe–S, and Fe–O) at 330 GPa (Fig. 5).

On the basis of these observations, Figs. 9a–d illustrate the liquidus phase relations (showing a compositional range from which a specific solid phase first crystallizes) in the Fe–C–X ternary systems at the ICB, with each ternary eutectic point located relatively close to the Fe–C binary eutectic point except for the Fe–C–H system.

Previous experiments and calculations have estimated the maximum amount of each light element in the liquid core to explain the outer core density deficit. Estimates based on liquid iron alloys show 4.6–6.4 wt.% Si (Morard et al., 2013; Badro et al., 2014), 5.8–14.0 wt.% S (Morard et al., 2013; Badro et al., 2014; Umemoto et al., 2014; Kawaguchi et al., 2017), 5.5 wt.% O (Badro et al., 2014), and 1.0 wt.% H (Umemoto and Hirose, 2015) at the ICB, which are again less than those obtained by the earlier study on the EoSs of solid FeSi, FeS, and Fe<sub>0.95</sub>O (Sata et al., 2010). These give the possible compositional range of Fe–C–X ternary outer core liquid in Figs. 9a–d (green area).

We find that hcp Fe crystallizes from possible liquid core compositions in all of the Fe–C–Si, Fe–C–S, Fe–C–O, and Fe–C–H systems. The recent calculations by Li et al. (2018) proposed that all of the density,  $V_P$ , and  $V_S$  of the solid inner core are explained by hcp Fe<sub>30</sub>C<sub>1</sub>Si<sub>1</sub> (Fe + 0.7 wt.% C + 1.6 wt.% Si). Such inner core composition is feasible, considering that the maximum solubilities of silicon and sulfur in hcp Fe when coexisting with liquid alloys are  $\leq 1.5$  wt.% Si and 4 wt.% S at the ICB, respectively (Ozawa et al., 2016; Mori et al., 2017). Hcp Fe + 1 wt.% C + 4.0 wt.% S also could account for the inner core density (Sakai et al., 2012). Hydrogen is known to be soluble in solid Fe (Fukai, 1992; Shibazaki et al., 2012; Terasaki et al., 2012), suggesting that the hcp Fe–C–H inner core is also feasible. On the other hand, solid Fe crystallizing from liquid Fe–C–O contains  $\leq 1$  wt.% carbon and a negligible amount of oxygen (Ozawa et

al., 2010), which does not account for the inner core density deficit (Li et al., 2018).

Therefore, while carbon is not a predominant light element in the core, the outer core liquid can be Fe-C-Si, Fe-C-S, or Fe-C-H.

## **5. Conclusion**

We have conducted melting experiments on the Fe–C binary system up to 255 GPa by using a laser-heated DAC. The carbon concentration in eutectic liquid and the solubility of carbon in solid iron were determined based on textual and chemical characterizations for samples recovered from the DAC. Results show that 1) the carbon content in eutectic liquid slightly decreases with increasing pressure from 4.3 wt.% C at ambient pressure to 3.6 wt.% C at 255 GPa, 2) eutectic melting occurs between Fe and Fe<sub>3</sub>C to 203 GPa and between Fe and Fe<sub>7</sub>C<sub>3</sub> at 255 GPa, and 3) the maximum solubility of carbon in solid iron is almost constant ( $\leq 1$  wt.%) up to 255 GPa. The eutectic liquid in the Fe–C binary system includes about 3 wt.% C at 330 GPa.

If carbon is the sole light element in the core and the outer core includes  $<3$  wt.% C, hcp Fe crystallizes at the ICB but includes only less than 1 wt.% C, which does not explain the inner core density deficit. If the liquid core contains more than 3 wt.% C, it forms Fe<sub>7</sub>C<sub>3</sub> at the ICB, whose density is too low for the inner core. These indicate that carbon is not a primary light element in the core. On the other hand, the outer core can be liquid Fe-C-Si, Fe-C-S, or Fe-C-H. It crystallizes hcp Fe including light elements with less than 1 wt.% C, which may explain the density and the sound velocities observed in the inner core.

## **Acknowledgments**

We appreciate Y. Nakajima for his help in quantitative determination of carbon content with an EPMA. We also thank K. Yonemitsu, H. Yoshida, S. Tagawa, S. Tateno, and Y. Kuwayama for their support during experiments. Comments provided by anonymous reviewers were helpful, in particular on the EPMA analysis of carbon. This work was supported by the JSPS research grant 16H06285 to K.H. XRD measurements were performed at BL10XU, SPring-8 (proposals no. 2017A0072 and 2017B0072). F.M. and G.M. received funding from the European Research Council (ERC) under the European Union's Horizon 2020 research and innovation Programme (grant agreement no. 670787).

## References

- Akahama, Y., Kawamura, H., 2007. Diamond anvil Raman gauge in multimegabar pressure range. *High Press. Res.* 27, 473–482.  
<https://doi.org/10.1080/08957950701659544>
- Anders, E., Grevesse, N., 1989. Abundances of the elements: meteoritic and solar. *Geochim. Cosmochim. Acta* 53, 197–214. [https://doi.org/10.1016/0016-7037\(89\)90286-X](https://doi.org/10.1016/0016-7037(89)90286-X)
- Andraut, D., Fiquet, G., Itie, J.P., Richet, P., Gillet, P., Hausermann, D., Hanfland, M., 1998. Thermal pressure in the laser-heated diamond-anvil cell: an X-ray diffraction study. *Eur. J. Mineral.* 10, 931–940.
- Anzellini, S., Dewaele, A., Mezouar, M., Loubeyre, P., Morard, G., 2013. Melting of iron at earth's inner core boundary based on fast X-ray diffraction. *Science* 340, 464–466. <https://doi.org/10.1126/science.1233514>
- Badro, J., Cote, A.S., Brodholt, J.P., 2014. A seismologically consistent compositional model of Earth's core. *Proc. Natl. Acad. Sci. USA* 111, 7542–7545.  
<https://doi.org/10.1073/pnas.1316708111>
- Benz, M., Elliott, J., 1961. The austenite solidus and revised iron-carbon diagram. *Trans. Metall. Soc. AIME* 221, 323–331.
- Brown, J.M., McQueen, G., 1986. Phase transitions, Grüneisen parameter, and elasticity for shocked iron between 77 GPa and 400 GPa. *J. Geophys. Res.* 91, 7485–7494.  
<https://doi.org/10.1029/JB091iB07p07485>
- Chabot, N.L., Campbell, A.J., McDonough, W.F., Draper, D.S., Agee, C.B., Humayun, M., Watson, H.C., Cottrell, E., Saslow, S.A., 2008. The Fe–C system at 5 GPa and

implications for Earth's core. *Geochim. Cosmochim. Acta* 72, 4146–4158.  
<https://doi.org/10.1016/j.gca.2008.06.006>  
 Chen, B., Li, Z., Zhang, D., Liu, J., Hu, M.Y., Zhao, J., Bi, W., Alp, E.E., 2014. Hidden  
 carbon in Earth's inner core revealed by shear softening in dense Fe<sub>7</sub>C<sub>3</sub>. *Proc.*  
*Natl. Acad. Sci. USA* 111, 17755–17758. <https://doi.org/10.1073/pnas.1411154111>  
 Dasgupta, R., Walker, D., 2008. Carbon solubility in core melts in a shallow magma  
 ocean environment and distribution of carbon between the Earth's core and the  
 mantle. *Geochim. Cosmochim. Acta* 72, 4627–4641.  
<https://doi.org/10.1016/j.gca.2008.06.023>  
 Dewaele, A., Loubeyre, P., Occelli, F., Mezouar, M., Dorogokupets, P. I., Torrent, M.,  
 2006. Quasihydrostatic equation of state of iron above 2 Mbar. *Phys. Rev. Lett.* 97,  
 215504. <https://doi.org/10.1103/PhysRevLett.97.215504>  
 Fei, Y., Brosh, E., 2014. Experimental study and thermodynamic calculations of phase  
 relations in the Fe–C system at high pressure. *Earth Planet. Sci. Lett.* 408, 155–  
 162. <https://doi.org/10.1016/j.epsl.2014.09.044>  
 Fischer, R.A., Campbell, A.J., Reaman, D.M., Miller, N.A., Heinz, D.L., Dera, P.,  
 Prakapenka, V.B., 2013. Phase relations in the Fe–FeSi system at high pressures  
 and temperatures. *Earth Planet. Sci. Lett.* 373, 54–64.  
<https://doi.org/10.1016/j.epsl.2013.04.035>  
 Fukai, Y., 1992. Some properties of the Fe–H system at high pressures and  
 temperatures, and their implications for the Earth's core. In: Syono Y., Manghnani  
 M.H. (Eds.), *High-Pressure Research: Application to Earth and Planetary Sciences*.  
 AGU monogr. ser. 67, pp. 373–385. <https://doi.org/10.1029/GM067p0373>



431 Helffrich, G., 2014. Outer core compositional layering and constraints on core liquid  
 432 transport properties. *Earth Planet. Sci. Lett.* 391, 256–262.  
 433 <https://doi.org/10.1016/j.epsl.2014.01.039>

434 Hillgren, V.J., Gessmann, C.K., Li, J., 2000. An experimental perspective on the light  
 435 element in Earth's core. In: Canup, R.M., Richter, K. (Eds.), *Origin of the Earth*  
 436 *and Moon*. Univ. Arizona Press, pp. 245–263.

437 Hirose, K., Morard, G., Sinmyo, R., Umemoto, K., Hernlund, J.W., Labrosse, S., 2017.  
 438 Crystallization of silicon dioxide and compositional evolution of the Earth's core.  
 439 *Nature* 543, 99–102. <https://doi.org/10.1038/nature21367>

440 Ichikawa, H., Tsuchiya, T., Tange, Y., 2014. The P-V-T equation of state and  
 441 thermodynamic properties of liquid iron. *J. Geophys. Res. Solid Earth* 119, 240–  
 442 252. <https://doi.org/10.1002/2013JB010732>

443 Kawaguchi, S. I., Nakajima, Y., Hirose, K., Komabayashi, T., Ozawa, H., Tateno, S.,  
 444 Kuwayama, Y., Tsutsui, S., Baron, A.Q., 2017. Sound velocity of liquid Fe–Ni–S  
 445 at high pressure. *J. Geophys. Res. Solid Earth* 122, 3624–3634.  
 446 <https://doi.org/10.1002/2016JB013609>

447 Komabayashi, T., Fei, Y., 2010. Internally consistent thermodynamic database for iron  
 448 to the Earth's core conditions. *J. Geophys. Res. Solid Earth* 115, 1–12.  
 449 <https://doi.org/10.1029/2009JB006442>

450 Li, Y., Vočadlo, L., Brodholt, J., Wood, I.G., 2016. Thermoelasticity of Fe<sub>7</sub>C<sub>3</sub> under  
 451 inner core conditions. *J. Geophys. Res. Solid Earth* 121, 5828–5837.  
 452 <https://doi.org/10.1002/2016JB013155>

453 Li, Y., Vočadlo, L., Brodholt, J.P., 2018. The elastic properties of hcp-Fe alloys under  
 454 the conditions of the Earth's inner core. *Earth Planet. Sci. Lett.* 493, 118–127.  
 455 <https://doi.org/10.1016/j.epsl.2018.04.013>  
 456 Liu, J., Lin, J., Prakapenka, V.B., Prescher, C., Yoshino, T., 2016. Phase relations of  
 457  $\text{Fe}_3\text{C}$  and  $\text{Fe}_7\text{C}_3$  up to 185 GPa and 5200 K: implication for the stability of iron  
 458 carbide in the Earth's core. *Geophys. Res. Lett.* 43, 12415–12422.  
 459 <https://doi.org/10.1002/2016GL071353>.  
 460 Lord, O.T., Walter, M.J., Dasgupta, R., Walker, D., Clark, S.M., 2009. Melting in the  
 461 Fe–C system to 70 GPa. *Earth Planet. Sci. Lett.* 284, 157–167.  
 462 <https://doi.org/10.1016/j.epsl.2009.04.017>  
 463 Masters, G., Gubbins, D., 2003. On the resolution of density within the Earth. *Phys.*  
 464 *Earth Planet. Inter.* 140, 159–167. <https://doi.org/10.1016/j.pepi.2003.07.008>  
 465 McDonough, W.F., 2003. Compositional model for the Earth's core. In: Holland, H.,  
 466 Turekian, K. (Eds.), *Treatise on Geochemistry: 2nd Edition*. Elsevier Ltd., pp.  
 467 559–577. <https://doi.org/10.1016/B978-0-08-095975-7.00215-1>  
 468 Mookherjee, M., Nakajima, Y., Neumann, G.S., Glazyrin, K., Wu, X., Dubrovinsky, L.,  
 469 Mccammon, C., Chumakov, A., 2011. High-pressure behavior of iron carbide  
 470 ( $\text{Fe}_7\text{C}_3$ ) at inner core conditions. *J. Geophys. Res. Solid Earth* 116, 1–13.  
 471 <https://doi.org/10.1029/2010JB007819>  
 472 Morard, G., Andrault, D., Guignot, N., Siebert, J., Garbarino, G., Antonangeli, D., 2011.  
 473 Melting of Fe–Ni–Si and Fe–Ni–S alloys at megabar pressures: Implications for  
 474 the core-mantle boundary temperature. *Phys. Chem. Miner.* 38, 767–776.  
 475 <https://doi.org/10.1007/s00269-011-0449-9>

476 Morard, G., Siebert, J., Andrault, D., Guignot, N., Garbarino, G., Guyot, F.,  
 477 Antonangeli, D., 2013. The Earth's core composition from high pressure density  
 478 measurements of liquid iron alloys. *Earth Planet. Sci. Lett.* 373, 169–178.  
 479 <https://doi.org/10.1016/j.epsl.2013.04.040>  
 480 Morard, G., Andrault, D., Antonangeli, D., Nakajima, Y., Auzende, A.L., Boulard, E.,  
 481 Cervera, S., Clark, A., Lord, O.T., Siebert, J., Svitlyk, V., Garbarino, G., Mezouar,  
 482 M., 2017a. Fe–FeO and Fe–Fe<sub>3</sub>C melting relations at Earth's core-mantle  
 483 boundary conditions : Implications for a volatile-rich or oxygen-rich core. *Earth*  
 484 *Planet. Sci. Lett.* 473, 94–103. <https://doi.org/10.1016/j.epsl.2017.05.024>  
 485 Morard, G., Nakajima, Y., Andrault, D., Antonangeli, D., Auzende, A.L., Boulard, E.,  
 486 Cervera, S., Clark, A.N., Lord, O.T., Siebert, J., Svitlyk, V., Garbarino, G.,  
 487 Mezouar, M., 2017b. Structure and density of Fe–C liquid alloys under high  
 488 pressure. *J. Geophys. Res. Solid Earth* 122, 7813–7823.  
 489 <https://doi.org/10.1002/2017JB014779>  
 490 Mori, Y., Ozawa, H., Hirose, K., Sinmyo, R., Tateno, S., Morard, G., Ohishi, Y., 2017.  
 491 Melting experiments on Fe–Fe<sub>3</sub>S system to 254 GPa. *Earth Planet. Sc. Lett.* 464,  
 492 135–141. <https://doi.org/10.1016/j.epsl.2017.02.021>  
 493 Nakajima, Y., Takahashi, E., Suzuki, T., Funakoshi, K., 2009. “Carbon in the core”  
 494 revisited. *Phys. Earth Planet. Inter.* 174, 202–211.  
 495 <https://doi.org/10.1016/j.pepi.2008.05.014>  
 496 Nakajima, Y., Imada, S., Hirose, K., Komabayashi, T., Ozawa, H., Tateno, S., Tsutsui,  
 497 S., Kuwayama, Y., Baron, A.Q.R., 2015. Carbon-depleted outer core revealed by  
 498 sound velocity measurements of liquid iron-carbon alloy. *Nat. Commun.* 6, 1–7.  
 499 <https://doi.org/10.1038/ncomms9942>

500 Ohishi, Y., Hirao, N., Sata, N., Hirose, K., Takata, M., 2008. Highly intense  
 501 monochromatic X-ray diffraction facility for high-pressure research at SPring-8.  
 502 High Press. Res. 28, 163–173. <https://doi.org/10.1080/08957950802208910>  
 503 Ozawa, H., Hirose, K., Tateno, S., Sata, N., Ohishi, Y. 2010. Phase transition boundary  
 504 between B1 and B8 structures of FeO up to 210 GPa. Phys. Earth Planet. Inter.  
 505 179, 157–163. <https://doi.org/10.1016/j.pepi.2009.11.005>  
 506 Ozawa, H., Hirose, K., Yonemitsu, K., Ohishi, Y., 2016. High-pressure melting  
 507 experiments on Fe–Si alloys and implications for silicon as a light element in the  
 508 core. Earth Planet. Sci. Lett. 456, 47–54. <https://doi.org/10.1016/j.epsl.2016.08.042>  
 509 Prescher, C., Dubrovinsky, L., Bykova, E., Kuzenko, I., Glazyrin, K., Kantor, A.,  
 510 McCammon, C., Mookherjee, M., Nakajima, Y., Miyajima, N., Sinmyo, R.,  
 511 Cerantola, V., Dubrovinskaia, N., Prakapenka, V., Rüffer, R., Chumakov, A.,  
 512 Hanfland, M., 2015. High Poisson's ratio of Earth's inner core explained by carbon  
 513 alloying. Nat. Geosci. 8, 220–223. <https://doi.org/10.1038/ngeo2370>  
 514 Sakai T., Ohtani, E., Kamada, S., Terasaki, H., Hirao, N. 2012. Compression of  
 515 Fe<sub>88.1</sub>Ni<sub>9.1</sub>S<sub>2.8</sub> alloy up to the pressure of Earth's inner core. J. Geophys. Res. Solid  
 516 Earth 117, B02210. <https://doi.org/10.1029/2011JB008745>  
 517 Sakamaki, T., Ohtani, E., Fukui, H., Kamada, S., Takahashi, S., Sakairi, T., Takahata,  
 518 A., Sakai, T., Tsutsui, S., Ishikawa, D., Shiraishi, R., Seto, Y., Tsuchiya, T., Baron,  
 519 A.Q.R., 2016. Constraints on Earth's inner core composition inferred from  
 520 measurements of the sound velocity of hcp-iron in extreme conditions. Sci. Adv. 2,  
 521 e1500802–e1500802. <https://doi.org/10.1126/sciadv.1500802>  
 522 Sata, N., Hirose, K., Shen, G., Nakajima, Y., Ohishi, Y., Hirao, N., 2010. Compression  
 523 of FeSi, Fe<sub>3</sub>C, Fe<sub>0.95</sub>O, and FeS under the core pressures and implication for light

524 element in the Earth's core. *J. Geophys. Res. Solid Earth* 115, 1–13.  
 525 <https://doi.org/10.1029/2009JB006975>  
 526 Seto, Y., Nishio-Hamane, D., Nagai, T., Sata, N., 2010. Development of a software  
 527 suite on X-ray diffraction experiments. *Rev. High Press. Sci. Technol.* 20, 269–  
 528 276. <https://doi.org/10.4131/jshpreview.20.269>  
 529 Shearer, P., Masters, G., 1990. The density and shear velocity contrasts at the inner core  
 530 boundary. *Geophys. J. Int.* 102, 408–491. [https://doi.org/10.1111/j.1365-](https://doi.org/10.1111/j.1365-246X.1990.tb04481.x)  
 531 [246X.1990.tb04481.x](https://doi.org/10.1111/j.1365-246X.1990.tb04481.x)  
 532 Shibazaki, Y., Ohtani, E., Fukui, H., Sakai, T., Kamada, S., Ishikawa, D., Tsutsui, S.,  
 533 Baron, A.Q.R., Nishitani, N., Hirao, N., Takemura, K., 2012. Sound velocity  
 534 measurements in dhcp-FeH up to 70 GPa with inelastic X-ray scattering:  
 535 implications for the composition of the Earth's core. *Earth Planet. Sci. Lett.* 313–  
 536 314, 79–85. <https://doi.org/10.1016/j.epsl.2011.11.002>  
 537 Shibazaki, Y., Terasaki, H., Ohtani, E., Tateyama, R., Nishida, K., Funakoshi, K., Higo,  
 538 Y., 2014. High-pressure and high-temperature phase diagram for Fe<sub>0.9</sub>Ni<sub>0.1</sub>–H  
 539 alloy. *Phys. Earth Planet. Inter.* 228, 192–201.  
 540 <https://doi.org/10.1016/j.pepi.2013.12.013>  
 541 Simon, F., Glatzel, G., 1929. Remarks on fusion pressure curve. *Z. Anorg. Allg. Chem.*  
 542 178, 309–316. <https://doi.org/10.1002/zaac.19291780123>  
 543 Tateno, S., Hirose, K., Ohishi, Y., Tatsumi, Y., 2010. The structure of iron in Earth's  
 544 inner core. *Science* 330, 359–361. <https://doi.org/10.1126/science.1194662>  
 545 Tateno, S., Kuwayama, Y., Hirose, K., Ohishi, Y. 2015. The structure of Fe–Si alloy in  
 546 Earth's inner core. *Earth Planet. Sci. Lett.* 418, 11–19.  
 547 <http://dx.doi.org/10.1016/j.epsl.2015.02.008>

548 Tateno, S., Hirose, K., Sinmyo, R., Morard, G., Hirao, N., Ohishi, Y., 2018. Melting  
 549 experiments on Fe–Si–S alloys to core pressures: silicon in the core? *Am. Miner.*  
 550 103, 742–748. <http://doi.org/10.2138/am-2018-6299>  
 551 Terasaki, H., Ohtani, E., Sakai, T., Kamada, S., Asanuma, H., Shibazaki, Y., Hirao, N.,  
 552 Sata, N., Ohishi, Y., Sakamaki, T., Suzuki, A., Funakoshi, K., 2012. Stability of  
 553 Fe–Ni hydride after the reaction between Fe–Ni alloy and hydrous phase ( $\delta$ -  
 554  $\text{AlOOH}$ ) up to 1.2Mbar: possibility of H contribution to the core density deficit.  
 555 *Phys. Earth Planet. Inter.* 194–195, 18–24.  
 556 <https://doi.org/10.1016/j.pepi.2012.01.002>  
 557 Umemoto, K., Hirose, K., 2015. Liquid iron–hydrogen alloys at outer core conditions  
 558 by first-principles calculations. *Geophys. Res. Lett.* 42, 7513–7520.  
 559 <https://doi.org/10.1002/2015GL065899>  
 560 Umemoto, K., Hirose, K., Imada, S., Nakajima, Y., Komabayashi, T., Tsutsui, S.,  
 561 Baron, A.Q.R., 2014. Liquid iron–sulfur alloys at outer core conditions by first-  
 562 principles calculations. *Geophys. Res. Lett.* 41, 6712–6717.  
 563 <https://doi.org/10.1002/2014GL061233>  
 564 Walker, D., Dasgupta, R., Li, J., Buono, A., 2013. Nonstoichiometry and growth of  
 565 some Fe carbides. *Contrib. Mineral. Petrol.* 166, 935–957.  
 566 <https://doi.org/10.1007/s00410-013-0900-7>  
 567 Wood, B.J., 1993. Carbon in the core. *Earth Planet. Sci. Lett.* 117, 593–607.  
 568 Wood, B.J., Li, J., Shahr, A., 2013. Carbon in the core : its influence on the properties  
 569 of core and mantle. In: Hazen, R.M., Jones, A.P., Baross, J.A. (Eds.), *Carbon in*  
 570 *Earth. Rev. Mineral. Geochem.* 75, pp. 231–250.  
 571 <https://doi.org/10.2138/rmg.2013.75.8>

## Figure captions

**Fig. 1.** (a) Temperature profile and (b) composite X-ray maps for oxygen (red), carbon (purple), iron (green), and aluminum (light blue) for run #3 performed at 138 GPa (see Fig. S1 for raw radiation spectra). Homogeneous quenched liquid is found at the center (hot part) surrounded by solid layers of iron. A measured temperature profile is combined in (a), which provides temperature at the liquid/solid boundary.

**Fig. 2.** Typical melting texture of a quenched sample and composite X-ray maps for oxygen, carbon, aluminum, and iron for run #5 at 40 GPa. SIM, scanning ion microscope image; SL, secondary electron image; Comp, backscattered image. Homogeneous quenched liquid is found at the center surrounded by solid layers of Fe and Fe<sub>3</sub>C.

**Fig. 3.** Carbon concentrations in liquids obtained in this study. Liquid compositions are shown by triangles (blue) when coexisting with solid Fe, inverse triangles (purple) when in contact with Fe<sub>3</sub>C, squares (red) when both solid Fe and Fe<sub>3</sub>C were found, and a diamond (orange) when solid Fe and Fe<sub>7</sub>C<sub>3</sub> were formed. The triangles and inverse triangles give lower and upper bounds for carbon concentration in eutectic liquid, respectively. Open and cross symbols represent eutectic compositions reported by previous studies (Chabot et al., 2008; Lord et al., 2009; Fei and Brosh, 2014; Morard et al., 2017a). Green curve shows the change in eutectic liquid composition with increasing pressure.

**Fig. 4.** Carbon contents in solid iron found in this study. Closed symbols are the same as in Fig. 3. Previous reports on the maximum solubility of carbon in solid iron are shown by open symbols (Walker et al., 2013; Fei and Brosh, 2014).

**Fig. 5.** (a) Fe–Fe<sub>3</sub>C (or Fe–Fe<sub>7</sub>C<sub>3</sub> above 255 GPa) eutectic melting curve (orange) obtained in this study (closed symbols). It agrees well with the previously determined Fe–C melting curves by Morard et al. (2017a) (blue) and Liu et al. (2015) (green). Black dotted curve represents the solidus of Fe<sub>3</sub>C composition reported by Liu et al. (2016). Purple dashed curve shows the melting temperature of pure Fe (Anzellini et al., 2013). (b) Eutectic melting curve of the Fe–C system obtained in this study compared with those of the Fe–Fe<sub>3</sub>S (Mori et al., 2017), Fe–FeO (Morard et al., 2017a), and Fe–FeSi (Fischer et al., 2013) binary systems.

**Fig. 6.** XRD patterns of Fe + 4.0 wt.% C obtained before and after heating (no melting), and during and after melting (a) at 203 GPa in run #7 and (b) 255 GPa in run #8. The unit-cell parameters and volumes of Fe<sub>3</sub>C and Fe<sub>7</sub>C<sub>3</sub> are  $a = 3.95(1) \text{ \AA}$ ,  $b = 4.54(1) \text{ \AA}$ ,  $c = 5.95(1) \text{ \AA}$ , and  $V = 106.9(4) \text{ \AA}^3$  for Fe<sub>3</sub>C, and  $a = 10.40(1) \text{ \AA}$ ,  $b = 3.96(1) \text{ \AA}$ ,  $c = 12.06(1) \text{ \AA}$ , and  $V = 496.4(3) \text{ \AA}^3$  for Fe<sub>7</sub>C<sub>3</sub>.

**Fig. 7.** Quenched textures and composite X-ray maps for carbon, oxygen, and iron at (a) 203 GPa (run #7) and (b) 255 GPa (run #8). While liquid was surrounded by Fe<sub>3</sub>C in the sample quenched at 203 GPa, it was in contact with Fe<sub>7</sub>C<sub>3</sub> and Fe at 255 GPa (the subsolidus part was composed of Fe<sub>3</sub>C and Fe).



**Fig. 8.** Phase diagrams for the iron-rich portion of the Fe–C binary system at 54, 138, 203, and 255 GPa from the present experiments and at ICB conditions (330 GPa) by extrapolation. Red and blue (and gray) curves represent Fe–Fe<sub>3</sub>C and Fe–Fe<sub>7</sub>C<sub>3</sub> eutectic, respectively.

**Fig. 9.** Likely liquidus phase relations in the Fe–C–X ternary systems at 330 GPa. Red circles represent the eutectic compositions in the Fe–C (this study), Fe–Si (Ozawa et al., 2016), Fe–S (Mori et al., 2017), Fe–O (Morard et al., 2017a), and Fe–H binary systems (Fukai, 1992). Green regions show the range of possible composition of the outer core that explains its density based on studies on liquid iron alloys (Morard et al., 2013; Badro et al., 2014; Umemoto et al., 2014; Umemoto and Hirose, 2015; Nakajima et al., 2015; Kawaguchi et al., 2017).

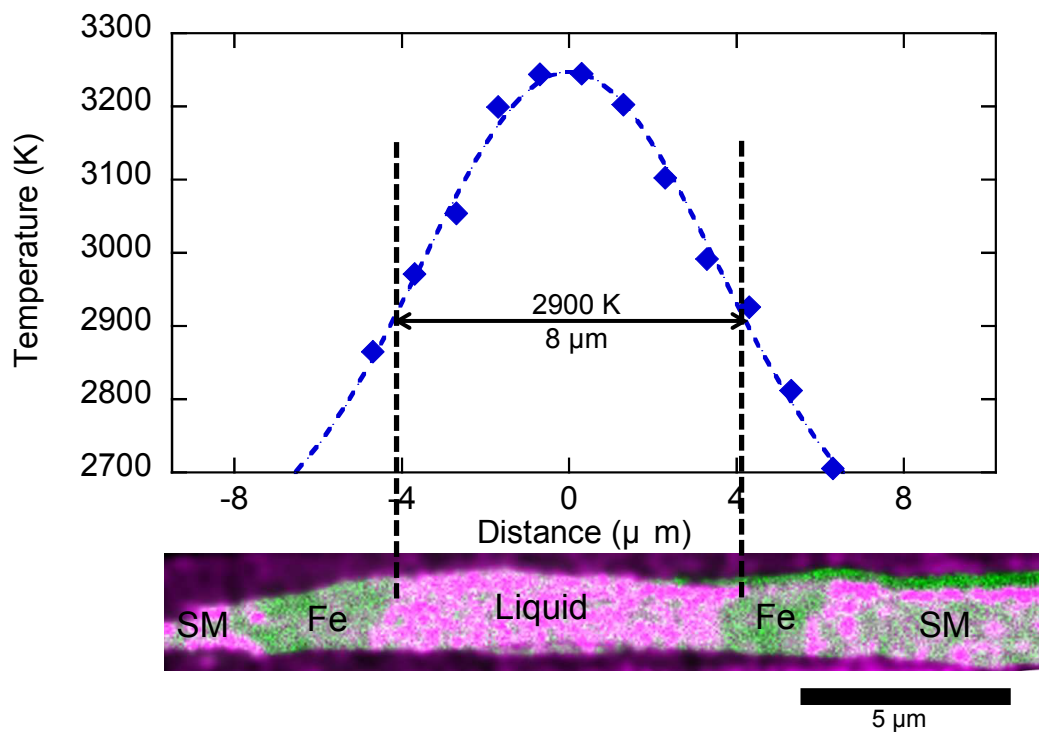
**Table 1**

Experimental results in the Fe-C binary system

Run#	Starting material	P (GPa)	eutectic T (K)	Phases present	Liquid		Solid iron	
					C (wt%)	Fe (wt%)	O (wt%)	C (wt%)
1	Fe-1.9 wt%C	23(2)	1950(100)	Liq + Fe	4.04(30)	96.30(30)	0.16(5)	0.85(24)
2	Fe-1.9 wt%C	54(5)	2550(130)	Liq + Fe + Fe <sub>3</sub> C	4.45(32)	95.70(30)	0.34(30)	1.00(45)
3	Fe-1.9 wt%C	138(14)	2900(150)	Liq + Fe	3.95(22)	94.84(21)	1.70(17)	0.68(48)
4	Fe-1.9 wt%C	211(21)	3230(160)	Liq + Fe + Fe <sub>3</sub> C	4.19(20)	95.23(30)	0.95(30)	1.04(22)
5	Fe-4.0 wt%C	40(4)	2300(120)	Liq + Fe + Fe <sub>3</sub> C	3.83(24)	96.50(23)	0.17(22)	0.64(4)
6	Fe-4.0 wt%C	83(8)	2640(130)	Liq + Fe <sub>3</sub> C	3.90(23)	95.72(12)	0.88(8)	-
7	Fe-4.0 wt%C	203(20)	3350(170)	Liq + Fe <sub>3</sub> C	3.92(9)	95.39(22)	1.19(21)	-
8	Fe-4.0 wt%C	255(25)	3570(180)	Liq + Fe + Fe <sub>7</sub> C <sub>3</sub>	3.60(21)	96.84(49)	1.06(50)	0.61(34)

Numbers in parentheses are standard deviation uncertainties in the last digit(s).

(a)



(b)

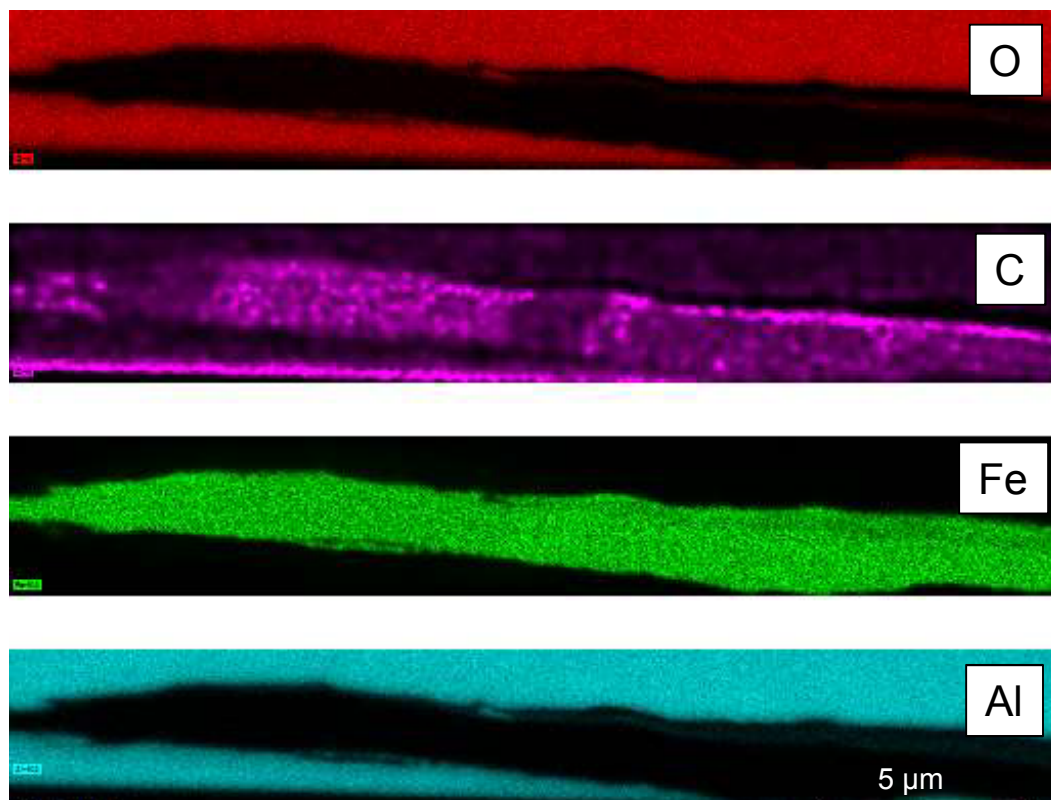


Fig. 1

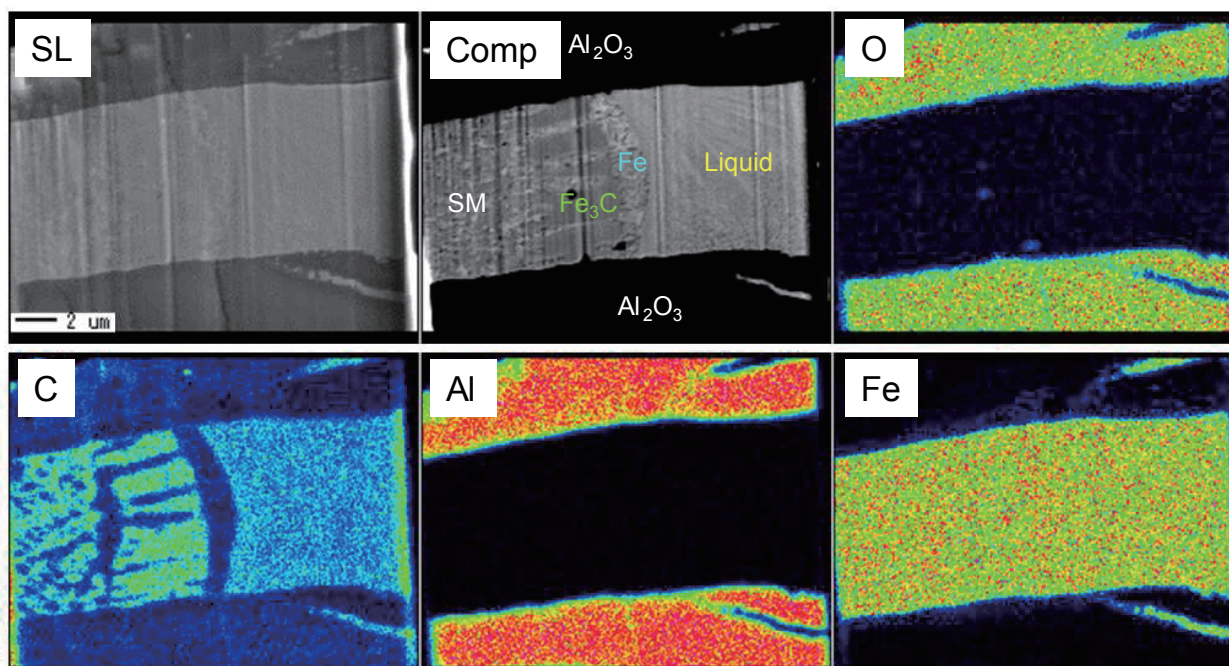
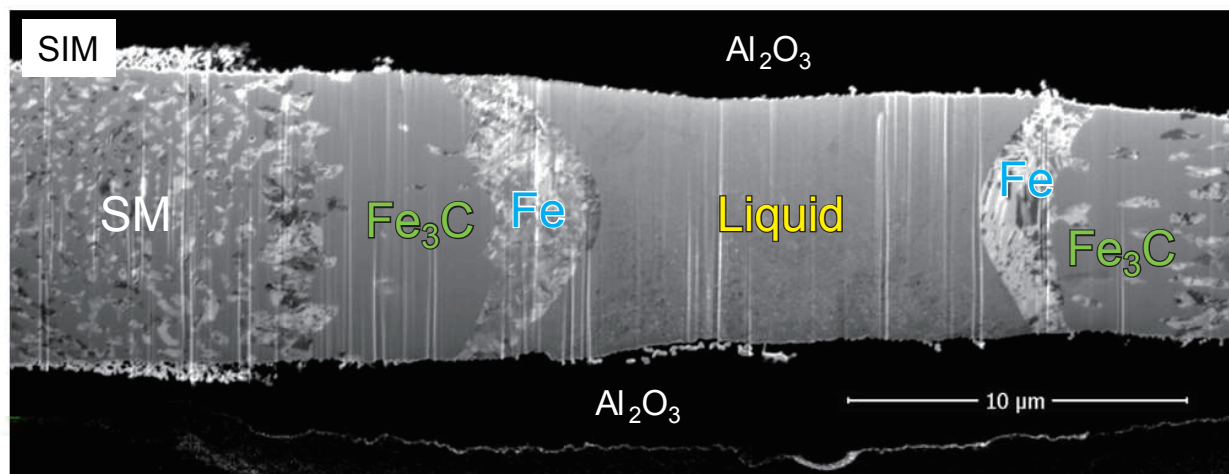


Fig. 2

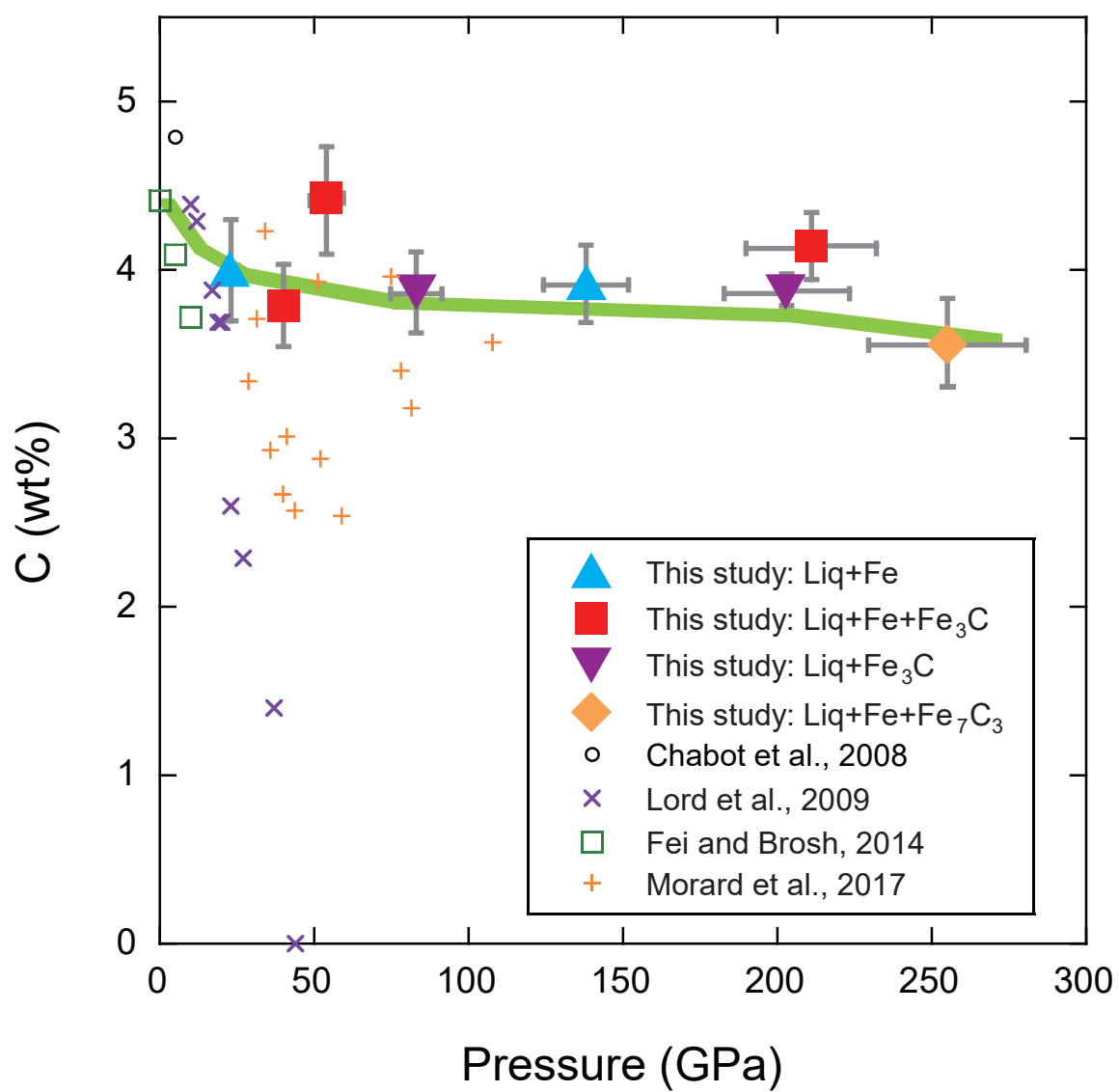


Fig. 3

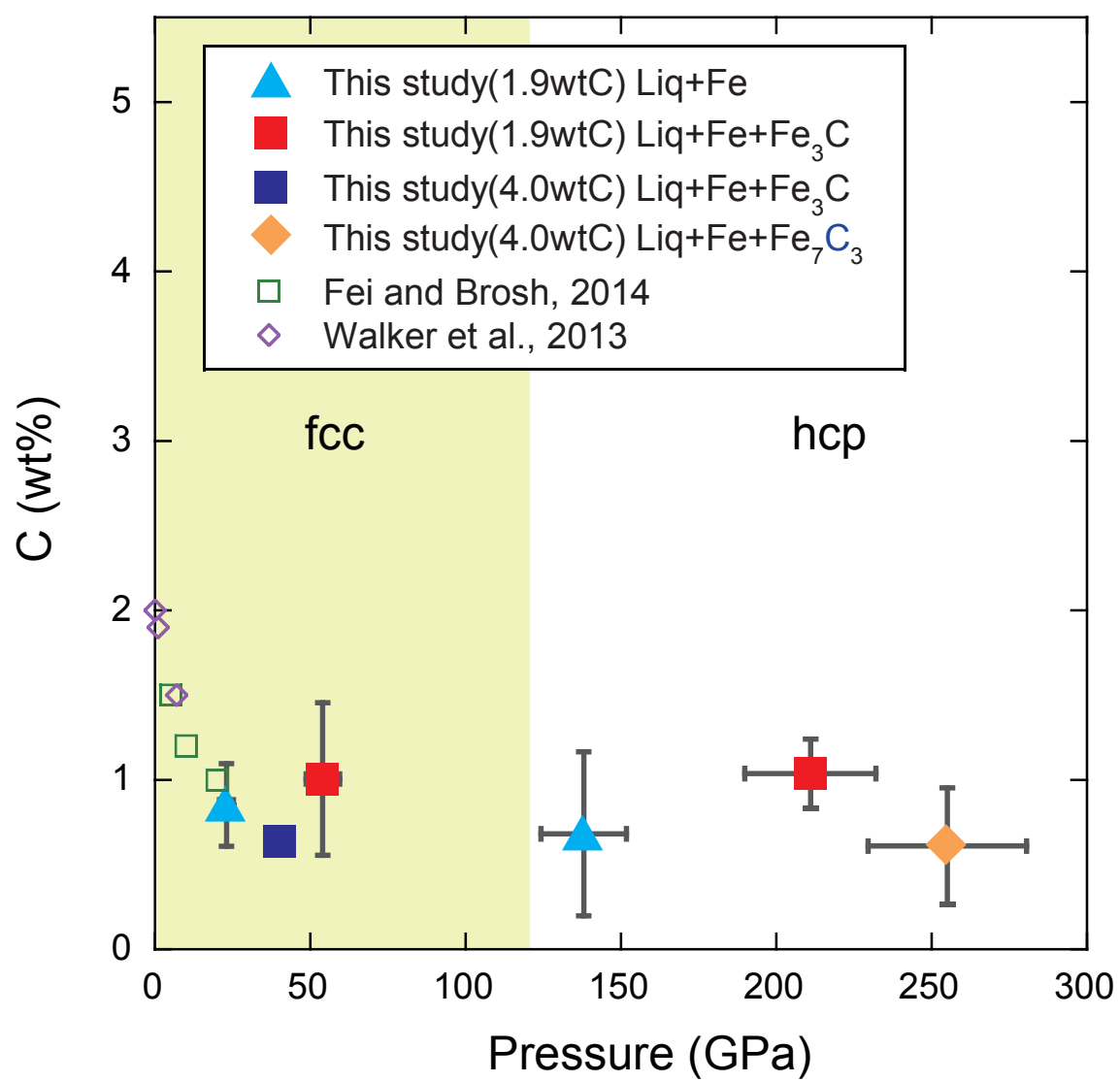


Fig. 4

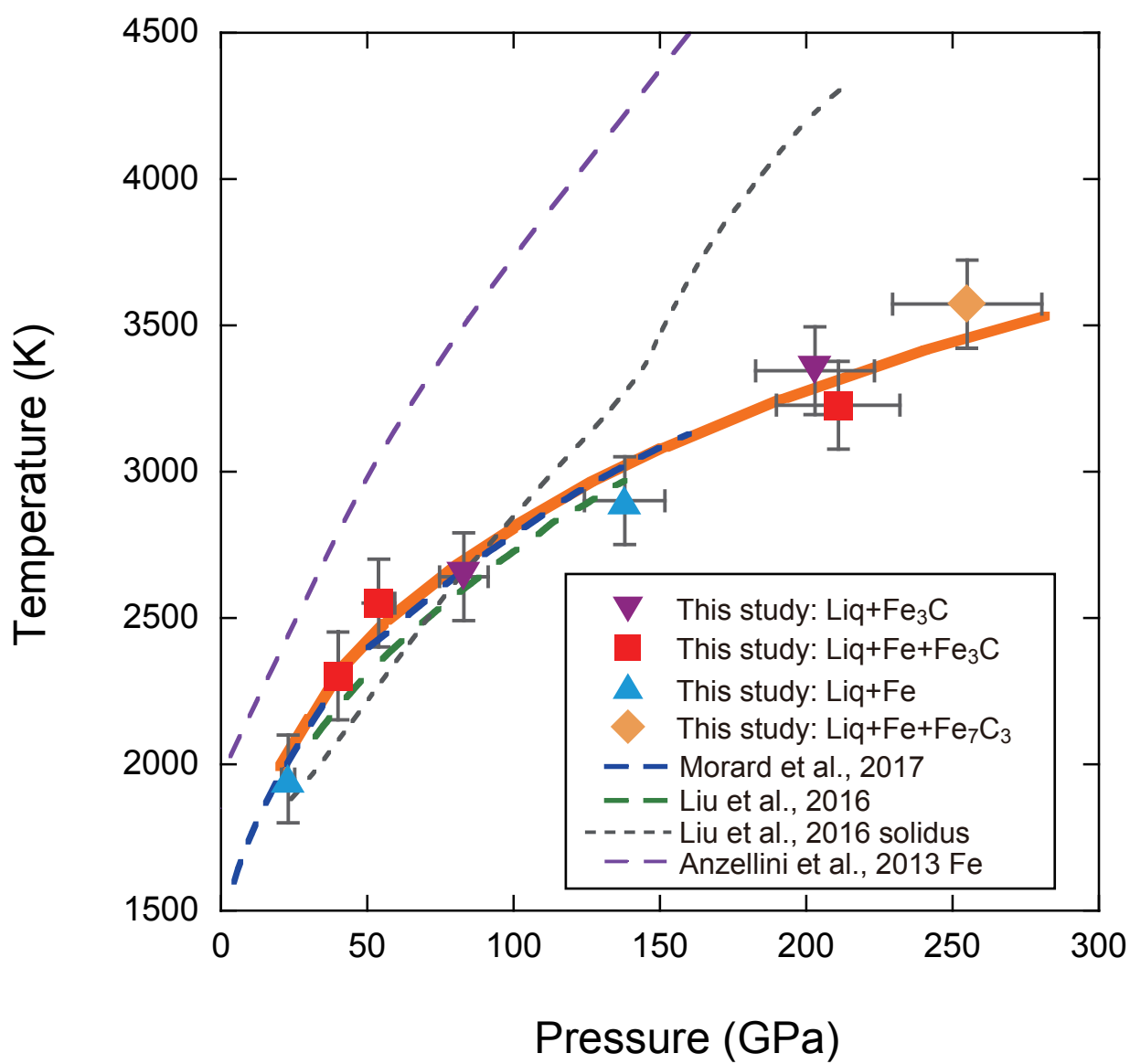


Fig. 5 (a)

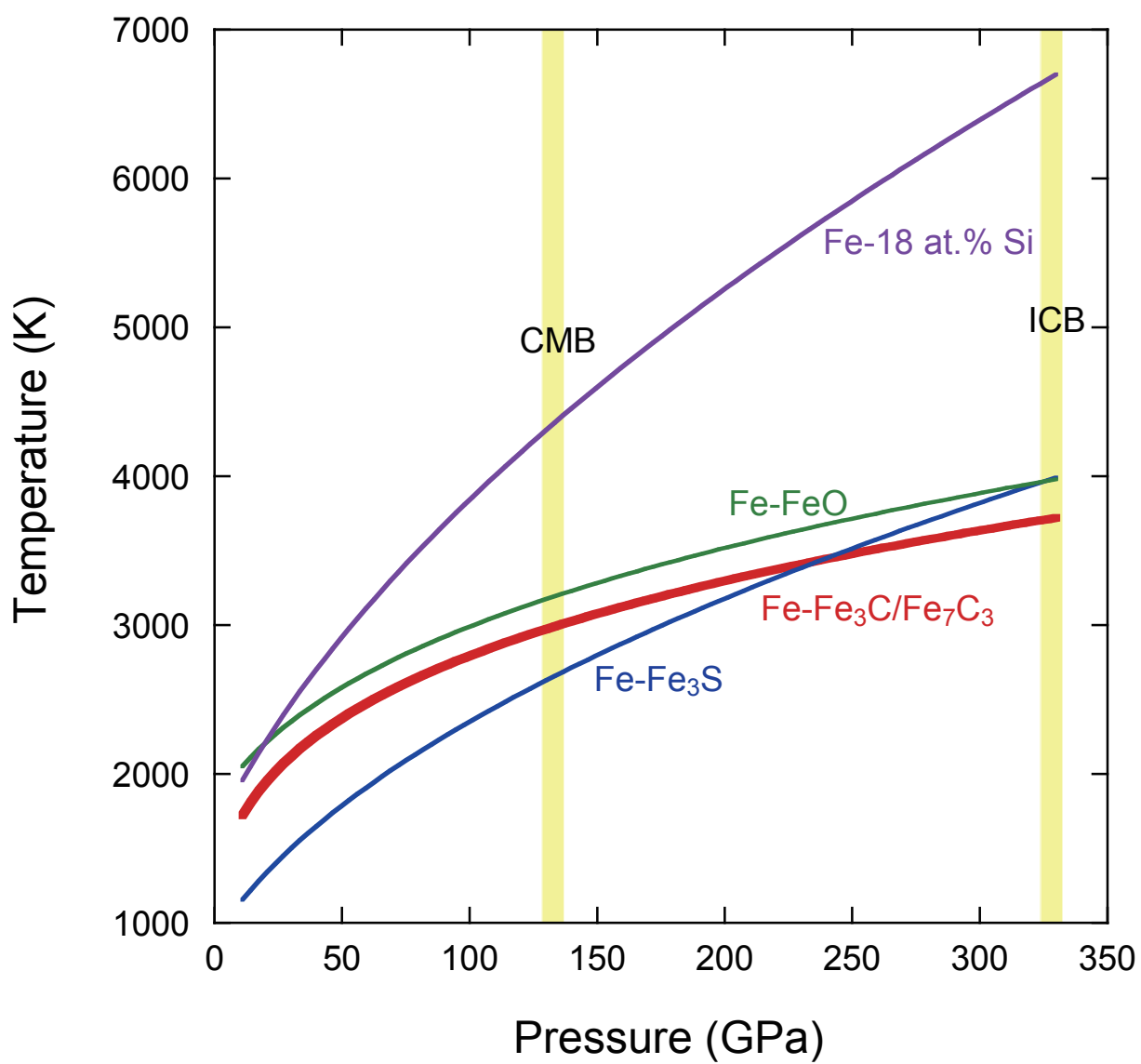


Fig. 5 (b)



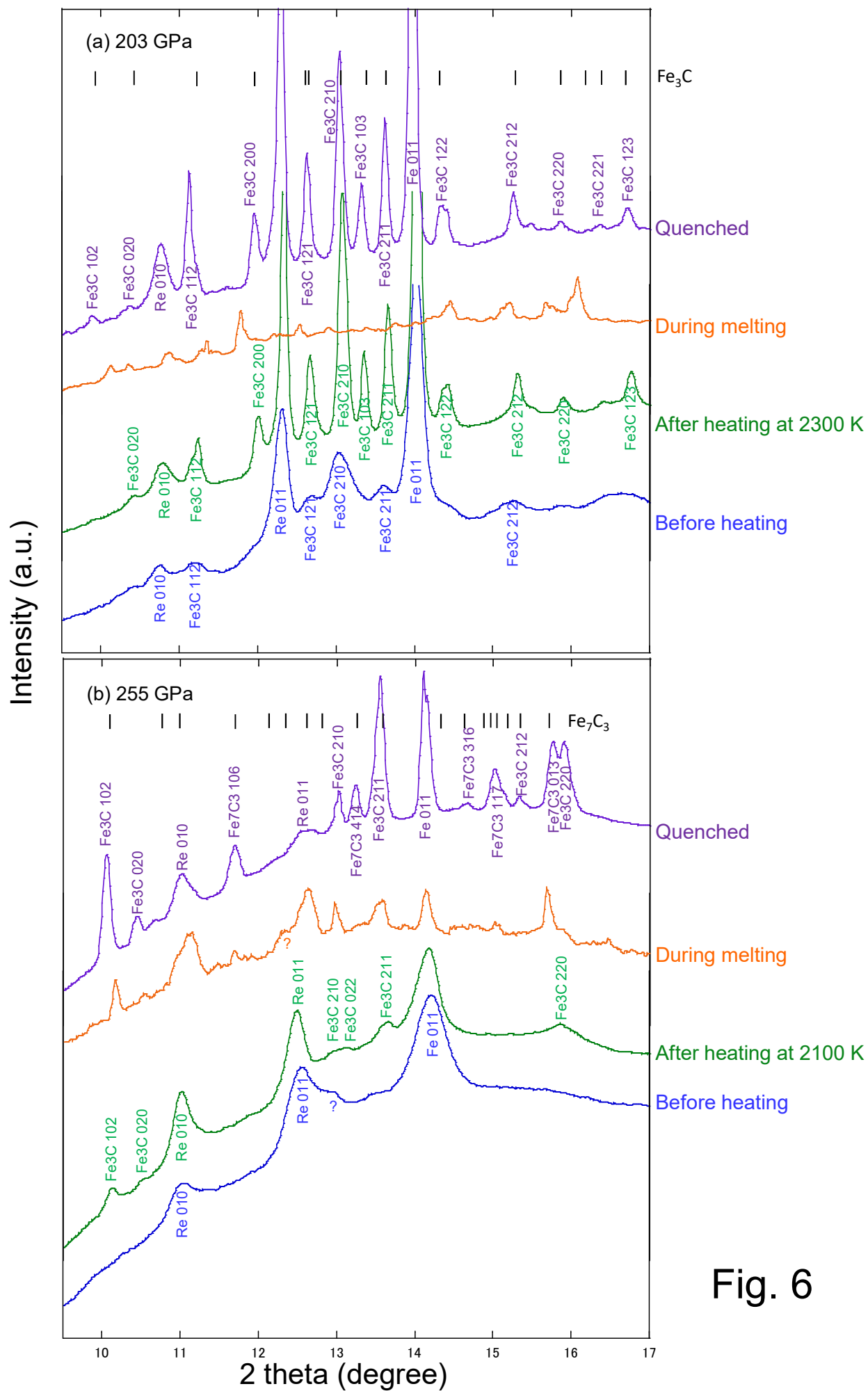
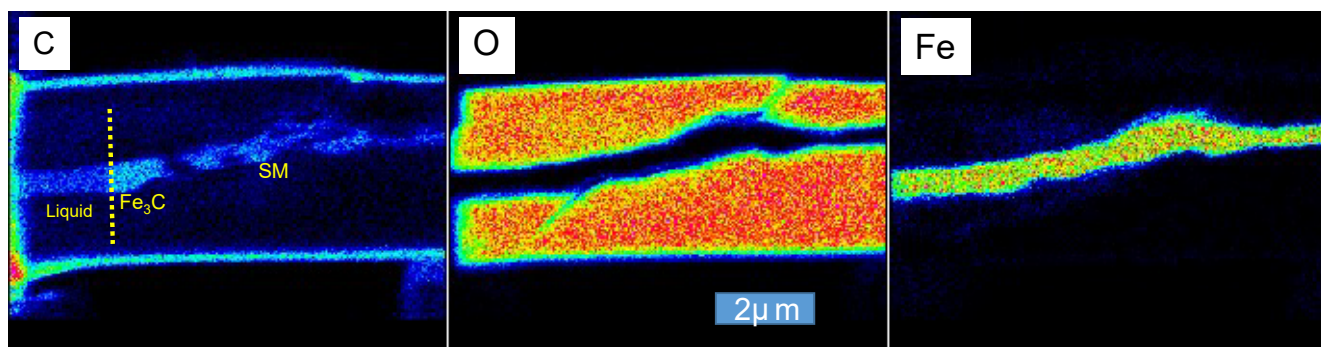
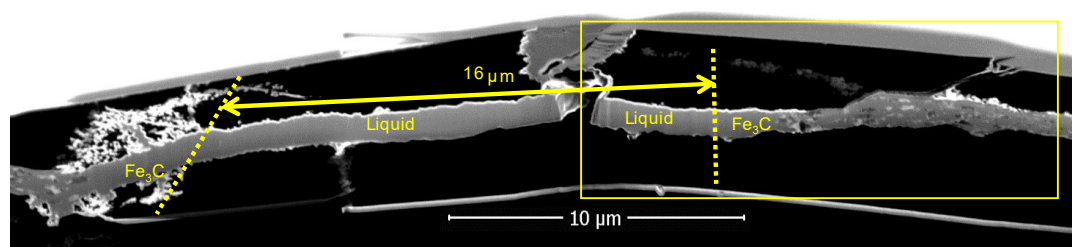


Fig. 6

(a)



(b)

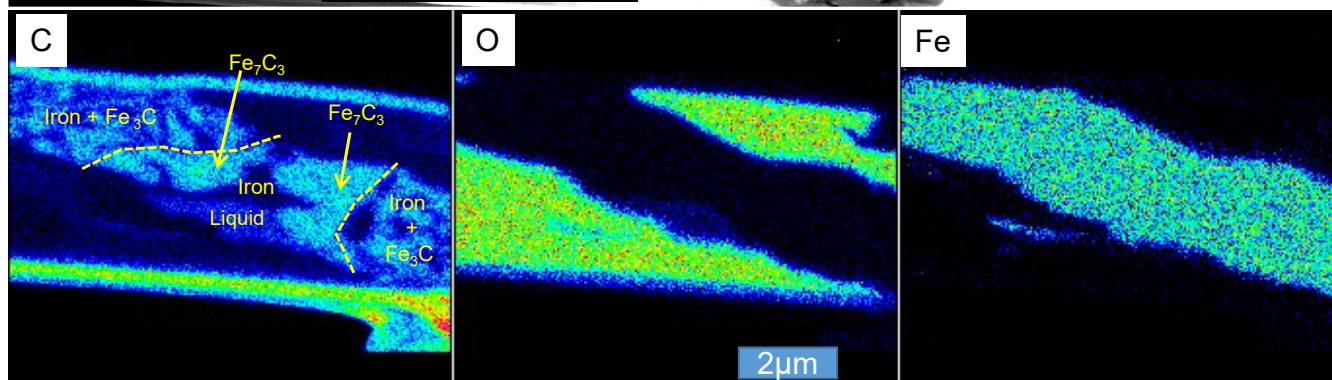
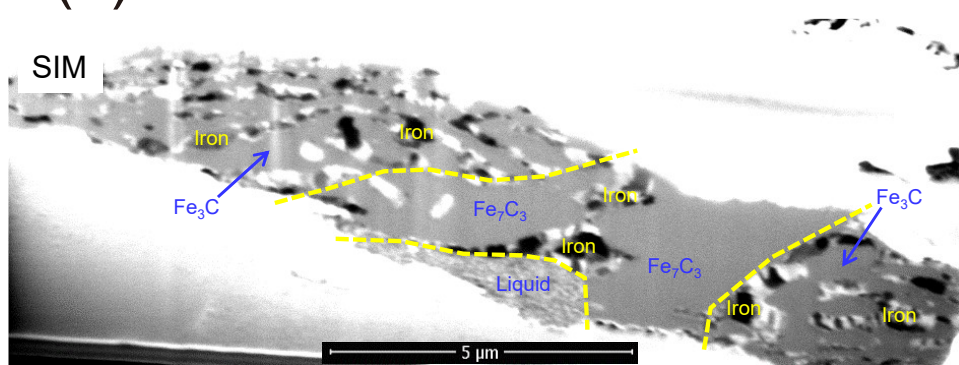


Fig. 7

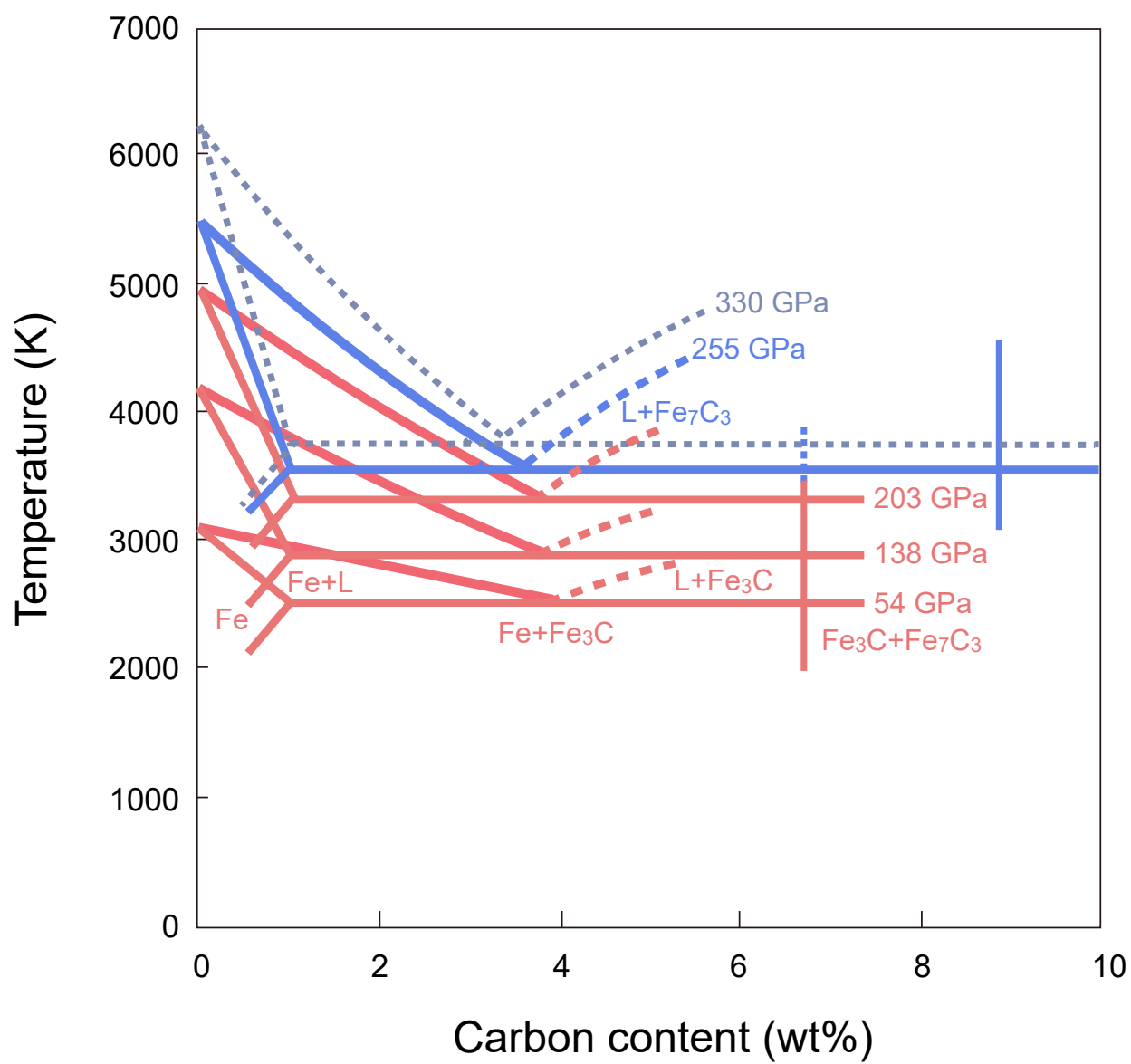


Fig. 8

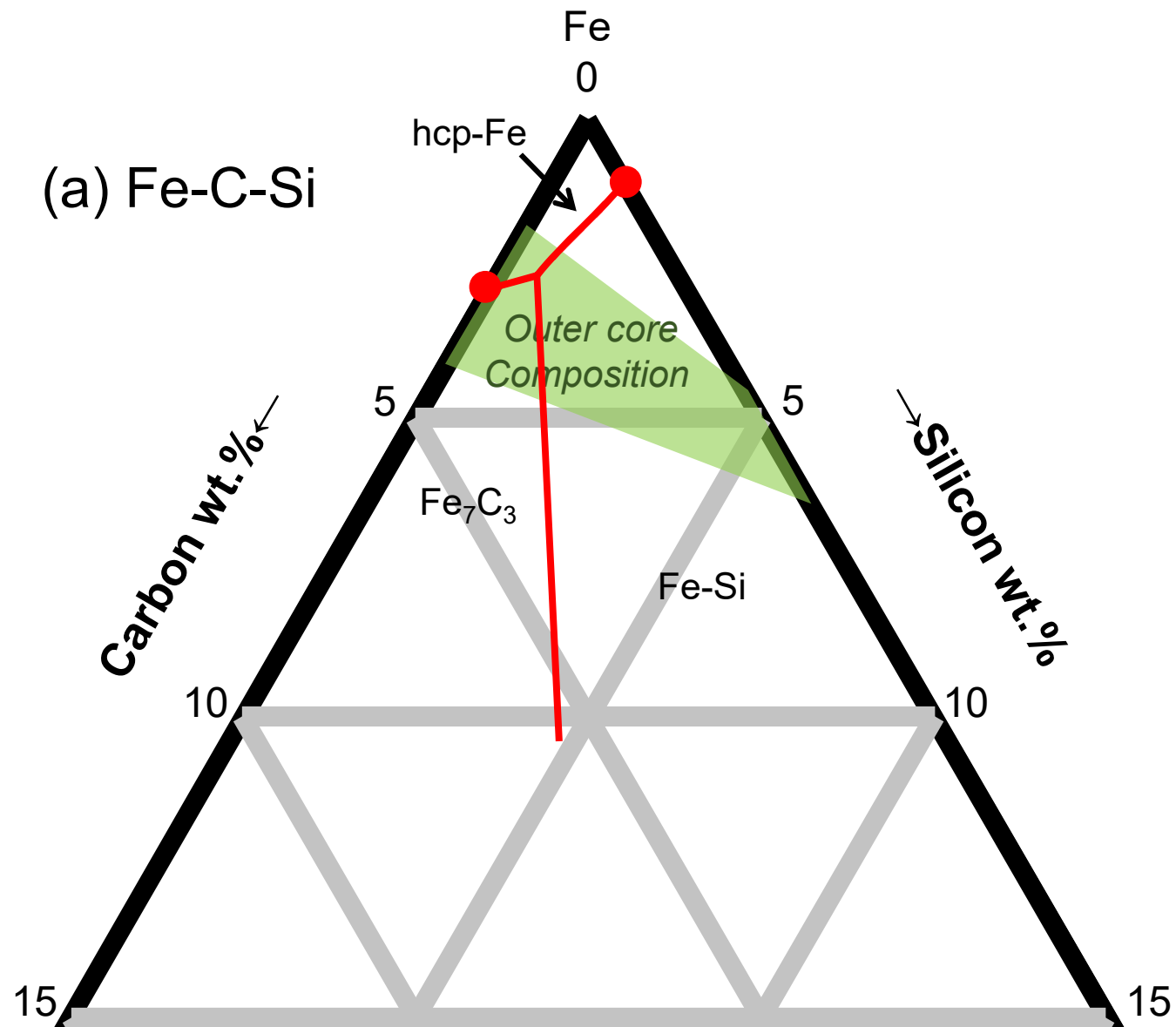


Fig. 9 (a)

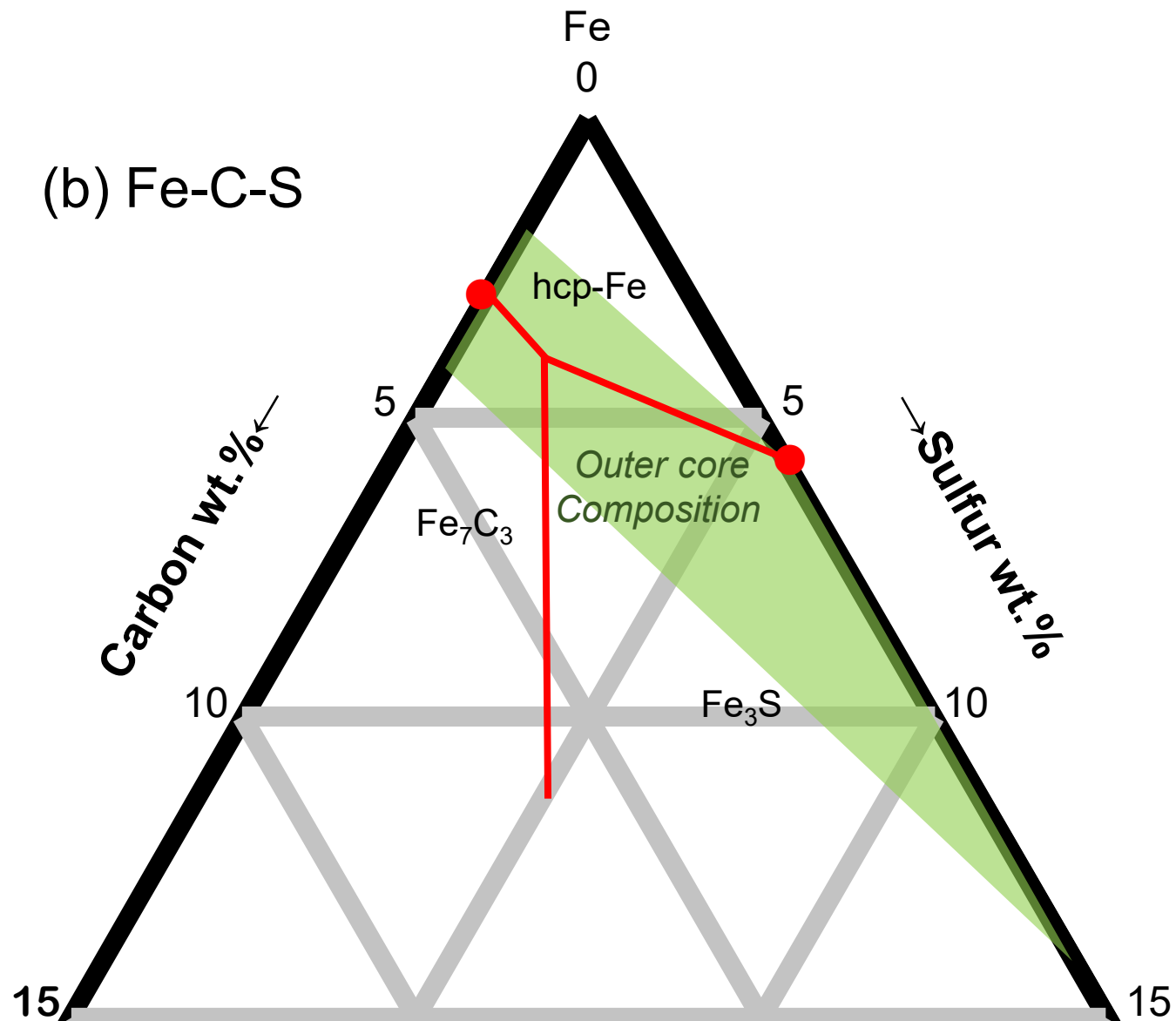


Fig. 9 (b)

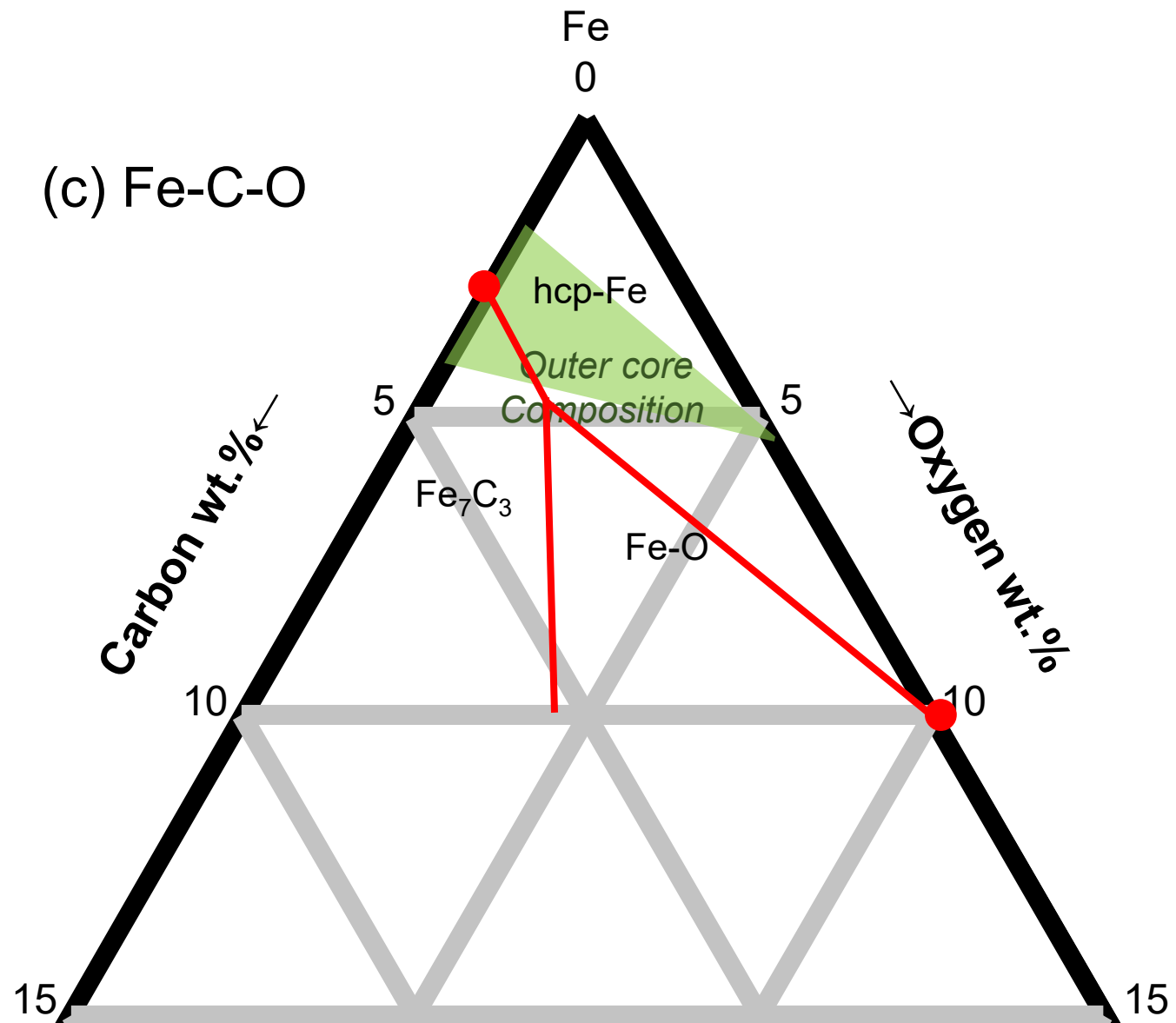


Fig. 9 (c)

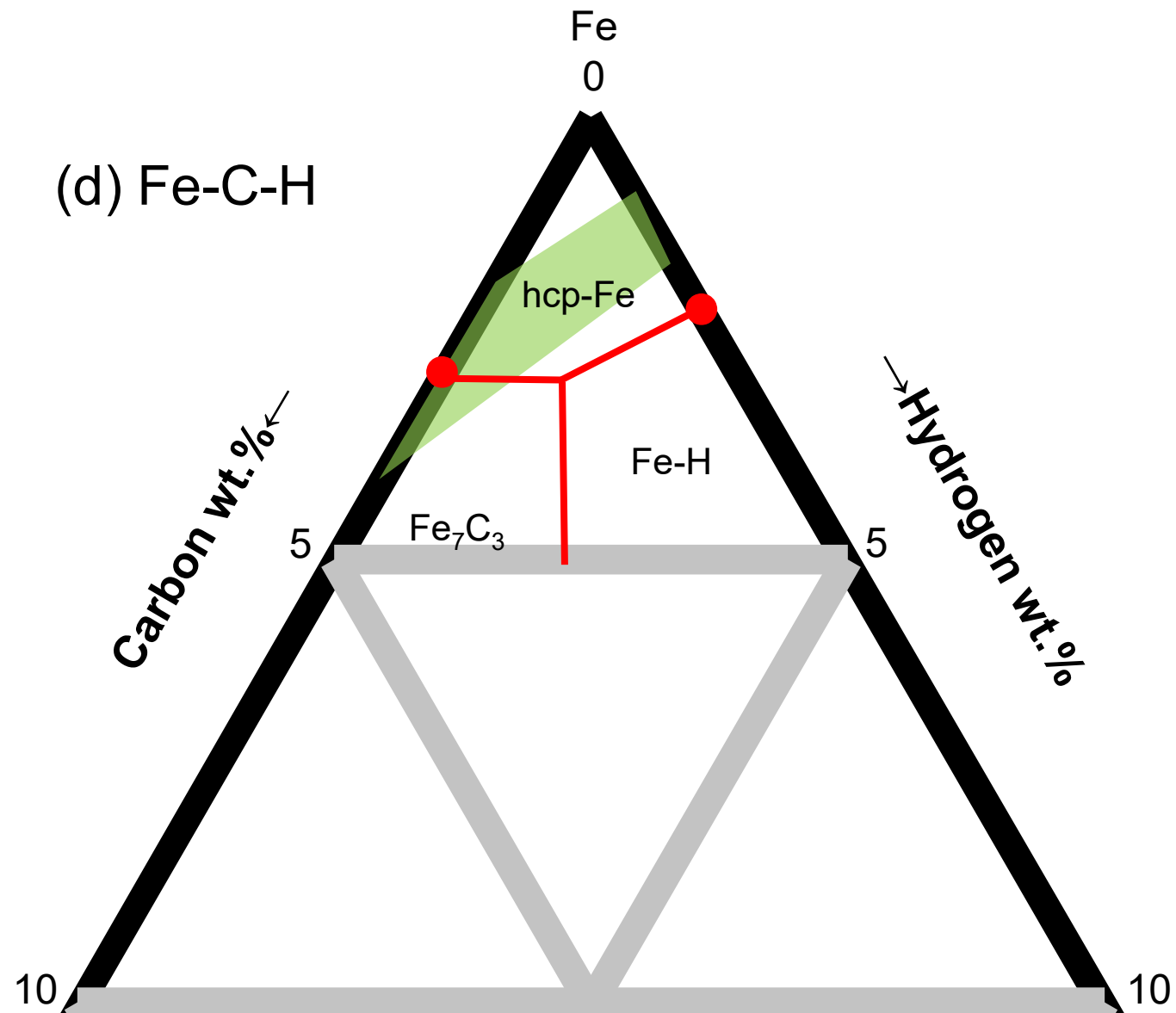


Fig. 9 (d)